Mixing and energy transfer in compressible Rayleigh-Taylor turbulence for initial isothermal stratification

Tengfei Luo⬛ and Jianchun Wang⬛*

Department of Mechanics and Aerospace Engineering, Southern University of Science and Technology,
Shenzhen 518055, China;
Southern Marine Science and Engineering Guangdong Laboratory (Guangzhou),
Guangzhou 511458, China;
and Guangdong-Hong Kong-Macao Joint Laboratory for Data-Driven Fluid Mechanics and Engineering
Applications, Southern University of Science and Technology, Shenzhen 518055, China

The effects of stratification parameter (Sr) and flow compressibility on mixing and energy transfer of three-dimensional compressible Rayleigh-Taylor turbulence are studied numerically for initial isothermal stratification at Sr. ranging from 0.5 to 3.0 and at Atwood number $A_t = 0.5$. Flow compressibility plays an important role in the generation of large-scale kinetic energy, which mainly comes from the conversion of potential energy for small Sr and conversion of internal energy through pressure-dilatation work for large Sr. The latter leads to that bubble heights increase rapidly and the bubbles are bigger at large Sr. The overall statistics of normalized subgrid-scale (SGS) flux of kinetic energy is nearly independent of Sr. The reverse SGS flux is much weaker than the direct SGS flux at middle scales, and increases significantly with increase of Sr. The net upscale cascade of kinetic energy can be identified at large scales, which is more obvious at larger Sr. The compression motions enhance direct SGS flux and the expansion motions strengthen the reverse SGS flux. The conditional average of SGS flux is nearly proportional to the normalized filtered velocity divergence at Sr $\leqslant$ 1.0 and the square of filtered velocity divergence at Sr > 2.0 in compression regions. The spatially average values of the large-scale pressure-dilatation are similar for different Sr and different times, and they have relatively large negative values at small scales for large Sr.

I. INTRODUCTION

Rayleigh-Taylor (RT) instability occurs when a light fluid supports a heavy fluid and there is an acceleration pointing to the light fluid. The small perturbations of the interface grow, interact nonlinearly, and eventually become turbulence. RT instability is of great importance in many engineering applications and natural phenomena, including inertial confinement fusion (ICF) [1,2] and type Ia supernova [3,4]. Compressibility plays a crucial role in supernova and ICF, which has been studied for many years [5,6].

For compressible RT instability, compressibility effects have two origins [7–10]: fluid compressibility, also called intrinsic compressibility, and flow compressibility, corresponding to the thermodynamic state of the system. The former is the inherent property of the fluid, which is characterized by the ratio of the specific heats γ of fluid [9,11]. The latter is related to the changes of fluid density [8,10,12], which is usually represented by stratification parameter Sr

---

*wangjc@sustech.edu.cn

or Mach number (Ma), where $Sr = Ma^2$. Flow compressibility results in an initial exponential density with height for initial isothermal stratification and a initial linear temperature for initial isopycnic stratification in the static state [7,13,14]. Its dynamic role is related to the expansion and compression motions, which associates with fluctuating of density of the fluid elements in response to change in pressure [15]. The expansion and compression motions can be quantified with turbulent Mach number, velocity divergence and dilatational component of velocity [16,17]. Therefore, the effect of stratification parameter or flow compressibility includes both static role and dynamic role.

The effect of flow compressibility on the spike height (the height of heavy fluid penetrating the lighter fluid) and bubble height (the height of light fluid penetrating the heavier fluid) at nonlinear stage in the two-dimensional (2D) single-mode RT instability has been widely studied, which depends on the initial thermodynamic equilibrium and Atwood number (A_t). Wieland et al. [13] numerically studied the compressible single-mode RT instability for initial isothermal, isentropic, and isopycnic background stratifications at $A_t = 0.4$ and different Mach numbers. They found that the bubble and spike heights develop at greater rates with higher Mach numbers in the nonlinear stage for initial isopycnic stratification, while they are suppressed for initial isothermal stratification. Luo et al. [7] numerically simulated 2D single-mode RT instability for initial isothermal stratification at different Mach numbers (Ma = $0.1 \sim 1.0$) and different Atwood numbers ($A_t = 0.1 \sim 0.9$). The bubble height is suppressed at small A_t and enhanced at large A_t with the increase in Ma, which is consistent with the observation by Reckinger et al. [8]. Luo et al. [7] reported that the initial density stratification caused by compressibility plays a stabilizing role and is dominant at small Atwood number ($A_t \leqslant 0.3$), while the expansion-compression motions of flow play a destabilizing role and are dominate at large Atwood number ($A_t \geqslant 0.7$). The competition between two effects determines the overall effect of compressibility. The numerical results at a range of Atwood number $A_t = 0.1 \sim 0.9$ of Fu et al. [18] were consistent with Luo et al. [7]. In addition, Fu et al. [18] reported a modified buoyancy-drag model for initial isothermal stratification, which gives an accurate analytical prediction of nonlinear saturation of bubble evolution, and verifies that expansion-compression motions play a destabilizing role for bubble evolution.

Luo and Wang [12] numerically studied the effects of Atwood number and stratification parameter on mixing heights in compressible 2D multimode RT turbulence, which are similar to the results of the single-mode RT instability. George and Glimm [19] reported a time-dependent Atwood number, which corresponds to the secondary growth rate of mixing height and self-similarity scaling law for highly compressible RT turbulence. Jin et al. [20] gave an analytical model based on the time-dependent Atwood number, which was verified at small A_t by numerical simulations. Jin et al. [20] and George and Glimm [19] pointed out that the dominant effect of compressibility was caused by the density stratification at small A_t. Some numerical results also showed that density stratification is dominant at $A_t = 0.25$ [10,21]. Gauthier [10] found that the bubble height no longer increases and spike height still grows at a very small rate during the freely decaying (FD) regime at $A_t = 0.25$ and large stratification parameter $Sr = 6.0$. In addition, the degree of molecular mixing grows continuously up to 0.99 during the FD regime, owing to that the mixing height stops growing and no more pure fluid enters in the mixing layer.

The kinetic energy transfer in incompressible RT flow was studied in the past. Cook and Zhou [22] numerically investigated the energy budget in incompressible RT turbulence. They found that the net kinetic energy transfer is from large scales to small scales, and depends strongly on the inhomogeneous direction. Because the diffusive mixing of the two unequal-density species leads to nonzero velocity divergence [12,23], dilatation term also exists in incompressible RT turbulence. They found that the energy transfer by the dilatation term is negligible, but its overall effect is to transfer energy from high density region to low density region. Cabot and Cook [24] found that the ratio of kinetic energy to released potential energy exhibits a gradual rise at late time, and finally reaches about 0.5 at the end of simulation. Cabot [25] also found that this ratio is about 0.5 in 3D, while it is 0.9 in 2D, which are basically consistent with 0.48 in 3D and 0.94 in 2D of Youngs [26]. Zhou et al. [27] investigated the scale-to-scale transport of kinetic energy in incompressible 2D RT

turbulence, by using a filtering approach. They revealed the upscale transfer of kinetic energy from small to large scales, due to the merging and grouping of buoyant structures.

Zhao *et al.* [14] numerically studied the kinetic energy transfer in compressible RT turbulence for initial isopycnic stratification at small Mach numbers Ma $\leqslant 0.55$. They presented the energy pathways between potential energy (PE), kinetic energy (KE), and internal energy (IE) in 3D compressible RT turbulence: PE and IE are converted to KE at the largest scale via gravity and pressure dilatation; the large-scale KE is then transferred to small scales by baropycnal work and deformation work though subgrid-scale flux of kinetic energy; finally, the small-scale KE converts to IE via viscous dissipation. The main difference between 3D and 2D RT turbulence is that deformation work transfers kinetic energy downscale in 3D and upscale in 2D, which can be used to explain the faster growth of the mixing height in 2D. In addition, baropycnal work and deformation work exhibit a self-similar evolution in time.

Zhao *et al.* [28] numerically investigated the kinetic energy transfer in 3D compressible RT turbulence for initial isothermal stratification at a Mach number of Ma $= 1.0$, using the single-species two-density model. They pointed that compressibility plays an important role for the generation and transfer of kinetic energy. There are two mechanisms for the generation of kinetic energy: the conversion of potential energy to kinetic energy and the pressure-dilatation work related to the compressibility of fluid elements. Energy transfer mainly depends on baropycnal work at large scale and deformation work at small scale. In addition, the negative baropycnal work is enhanced in the compression regions, while the positive baropycnal work is strengthened in the expansion regions. Luo and Wang [12] analyzed the kinetic energy equation in 2D compressible RT turbulence at different stratification parameters (Sr $= 0.1 \sim 1.0$) and Atwood numbers ($A_t = 0.2 \sim 0.8$), and found that the contribution of pressure-dilatation to the generation of kinetic energy is very important at large Sr. With an increase of Sr, the conversion of potential energy to kinetic energy weakens due to the density stratification, while pressure work increases owing to the significant expansion and compression motions.

The filtering techniques are often used to analyze interscale transfer of kinetic energy in turbulence. In constant density turbulence, the large-scale kinetic energy can be expressed as $|\bar{u}_\ell|^2/2$, where $\mathbf{u}$ is velocity and $\bar{f}_l$ is the filtered field of f at filter width l [see Eq. (21)]. There are several different definitions of large-scale kinetic energy in the variable density (VD) turbulence and compressible turbulence. Aluie proposed that the inviscid criterion, i.e., viscous effects are negligible at large scales, is important for the scale decomposition in the VD turbulence [29]. He proved theoretically that Favre decomposition satisfies the inviscid criterion for arbitrarily large density variations, which was verified numerically by Zhao and Aluie [30]. They also showed that two other commonly used decompositions in the literature, including $\bar{\rho}_\ell|\bar{\mathbf{u}}_\ell|^2/2$ [31,32] and $|\overline{(\sqrt{\rho}\mathbf{u})_\ell}|^2/2$ [22,33], can violate the inviscid criterion. Here, ρ is fluid density. In addition, Wang *et al.* [34] investigated the effect of different filter types on the kinetic energy transfer in compressible isotropic turbulence, by using top-hat filter, Gaussian filter, and sharp spectral filter. They found that the results of top-hat filter and Gaussian filter are similar to each other.

In this study, we investigate the effect of flow compressibility on the mixing and energy transfer in 3D compressible RT turbulence for isothermal background stratification at stratification parameters ranging from 0.5 to 3.0. We specifically focus on the generation of large-scale kinetic energy and the subgrid-scale (SGS) kinetic energy flux at different stratification numbers Sr. The rest of this paper is organized as follows. The next section presents the governing equations, initial and boundary conditions, and computational method. Section III provides the simulation parameters and statistics. Section IV describes the effect of compressibility on the mixing evolution. The effect of compressibility on energy transfer at different stratification numbers is presented in Sec. V. Finally, main conclusions are summarized in Sec. VI.

II. GOVERNING EQUATIONS AND NUMERICAL SIMULATIONS

A. Governing equations

A set of reference scales can be introduced to normalize the hydrodynamic and thermodynamic variables. The following reference variables are used: the reference length $L_r = L_x$, time $t_r = (L_x/g)^{1/2}$, velocity $u_r = (L_x g)^{1/2}$, density $\rho_r = (\rho_{H,0} + \rho_{L,0})/2$, temperature T_r, pressure $p_r = R\rho_r T_r/M_r$, concentration c_r, dynamic viscosity coefficient μ_r, thermal conductivity coefficient κ_r, diffusion coefficient of species D_r, specific heat at constant volume $C_{v,r}$, and molar weight $M_r = (M_H + M_L)/2$. g is the gravitational acceleration. $\rho_{H,0}$ and $\rho_{L,0}$ represent the densities on both sides of the initial interface. M_H and M_L are the molar masses of the heavy and light fluids, respectively. Subscripts H and L represent the heavy and light fluids, respectively [7,12].

The following dimensionless Navier-Stokes equations of compressible RT turbulence for a binary mixing fluid model of the miscible Newtonian fluids are solved numerically [7,10,12]:

$$\frac{\partial \rho}{\partial t} + \frac{\partial \rho u_j}{\partial x_j} = 0, \tag{1}$$

$$\frac{\partial \rho u_i}{\partial t} + \frac{\partial \rho u_i u_j}{\partial x_j} = -\frac{1}{\text{Sr}}\frac{\partial p}{\partial x_i} + \frac{1}{\text{Re}}\frac{\partial \sigma_{ij}}{\partial x_j} - \rho\delta_{i3}, \tag{2}$$

$$\frac{\partial \rho e}{\partial t} + \frac{\partial \rho e u_j}{\partial x_j} = -(\gamma_r - 1)p\frac{\partial u_j}{\partial x_j} + (\gamma_r - 1)\frac{\text{Sr}}{\text{Re}}\sigma_{ij}S_{ij} + \frac{\Delta_{H,L}^*}{\text{ReSc}}\frac{\partial}{\partial x_j}\left(\rho T \frac{\partial c}{\partial x_j}\right) + \frac{\gamma_r}{\text{RePr}}\frac{\partial}{\partial x_j}\left(\frac{\partial T}{\partial x_j}\right), \tag{3}$$

$$\frac{\partial \rho c}{\partial t} + \frac{\partial \rho c u_j}{\partial x_j} = \frac{1}{\text{ReSc}}\frac{\partial}{\partial x_j}\left(\rho\frac{\partial c}{\partial x_j}\right), \tag{4}$$

$$\frac{p}{\rho T} = \frac{1}{1 - A_t^2}(1 + A_t - 2A_t c), \tag{5}$$

where u_i is the velocity component, $\rho = \rho_H + \rho_L$ is the density, $p = p_H + p_L$ is the pressure, $T = T_H = T_L$ is the temperature, and $c = \rho_H/\rho$ is the concentrations of the heavy fluid. The viscous stress σ_{ij} is defined by

$$\sigma_{ij} = \mu\left(\frac{\partial u_i}{\partial x_j} + \frac{\partial u_j}{\partial x_i}\right) - \frac{2}{3}\mu\theta\delta_{ij}, \tag{6}$$

where $\mu = \mu_H = \mu_L$ is the dynamic viscosity. $\theta = \partial u_k/\partial x_k$ is the normalized velocity divergence. The internal energy per unit volume is defined by $e = C_v T$, where $C_v = cC_{v,H} + (1 - c)C_{v,L}$ is the specific heat at a constant volume. $\gamma_r = C_{p,r}/C_{v,r}$ is a reference variable of the ratio of specific heat at a constant pressure to that at a constant volume. $\Delta_{H,L}^* = \gamma_H C_{v,H} - \gamma_L C_{v,L}$ is the dimensionless difference in the specific heat at constant pressure [7,12], where $\gamma_{H,L}$ is the ratio of specific heat of heavy or light fluid.

The five reference governing parameters, including the stratification parameter Sr, Reynolds number Re, Atwood number A_t, Schmidt number Sc, and Prandtl number Pr, are [7,12]

$$\text{Sr} = \frac{gL_r}{RT_r/M_r}, \quad \text{Re} = \frac{g^{1/2}L_r^{3/2}}{\mu_r/\rho_r}, \quad A_t = \frac{M_H - M_L}{M_H + M_L}, \quad \text{Pr} = \frac{\gamma_r\mu_r C_{v,r}}{\kappa_r} \text{ and } \text{Sc} = \frac{\mu_r}{\rho_r D_r}. \tag{7}$$

Sr is related to the strength of flow compressibility (expansion and compression motions and density stratification). $c_0 = \sqrt{p_r/\rho_r} = \sqrt{RT_r/M_r}$ is the isothermal speed of sound. The Prandtl number and Schmidt number are assumed to be equal to 0.7 and 1.0, respectively. The Reynolds number is 10 000 in our simulations.
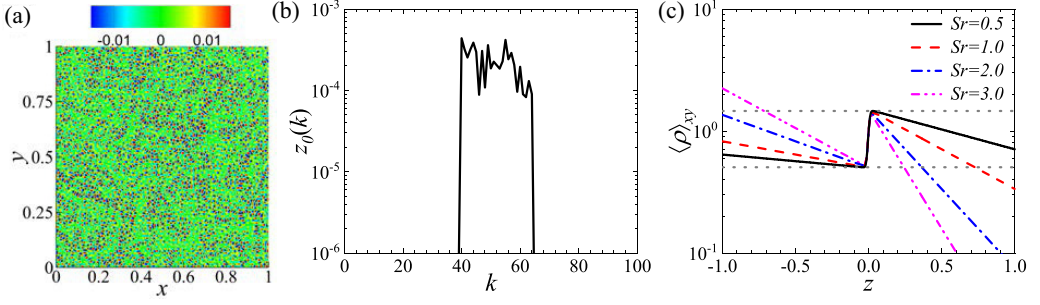
FIG. 1. (a) The initial perturbation displacement z_0, (b) the spectrum of initial perturbation displacement, and (c) the initial density profiles $\langle \rho \rangle_{xy}$ for different stratification parameters Sr. The dotted lines are the densities on both sides of the interface

B. Numerical simulations

We consider an isothermal background state with initial constant temperature of $T_0 = 1$. The density field for heavy and light fluids is exponential distribution. In our numerical simulations, the initial perturbation displacement z_0 is the superposition of sin and cos functions with different wave numbers [35–37]:

$$z_0(x_1, x_2) = \sum_{k_x, k_y} a_k \cos{(k_x x_1)} \cos{(k_y x_2)} + b_k \cos{(k_x x_1)} \sin{(k_y x_2)}$$
$$+ c_k \sin{(k_x x_1)} \cos{(k_y x_2)} + d_k \sin{(k_x x_1)} \sin{(k_y x_2)}, \tag{8}$$

where, a_k, b_k, c_k, d_k are random perturbation amplitudes and the r.m.s. amplitude $z_{0,\text{rms}} = 0.01$. The range of perturbation wave number is $40 \leqslant k = \sqrt{k_x^2 + k_y^2} \leqslant 64$. The interface perturbation in physical space and its spectrum are shown in Figs. 1(a) and 1(b), respectively. For ideal short wavelength perturbations, the influence of random initial perturbations can be ignored [35,37]. We have verified it in the Appendix.

To smooth the flow field at the interface between two fluids, we introduce regularized Heaviside functions, $H_{\pm}(x_3) = [1 \pm \text{erf}(x_3/\delta)]/2$, where $\text{erf}(x) = \frac{2}{\sqrt{\pi}} \int_0^x e^{-s^2} ds$, $\delta = 4\Delta$ is the pseudointerface thickness, and Δ is the grid spacing [7,12]. Then, we obtain the initial density field in the hydrostatic state:

$$\rho = (1 + A_t) \exp{[-\text{Sr}(1 + A_t)(x_3 - z_0)]} H_+(x_3 - z_0)$$
$$+ (1 - A_t) \exp{[-\text{Sr}(1 - A_t)(x_3 - z_0)]} H_-(x_3 - z_0). \tag{9}$$

The initial density profiles $\langle \rho \rangle_{xy}$ [see Eq. (11)] for different stratification parameters Sr are shown in Fig. 1(c). The initial pressure field and temperature field can be obtained by Eq. (2) and the equation of state.

For numerical simulations, we apply an eighth-order central compact finite difference scheme [38,39] on a uniform grid with $512^2 \times 1024$ grid points in a rectangular box of $L_r \times L_r \times 2L_r$ ($[-L_r, L_r]$), where $L_r = 1.0$. An eighth-order numerical hyper-viscosity model is adopted to ensure the stability of the algorithm [39]. A third-order Runge-Kutta scheme is applied for the time marching [40]. A sufficiently large wave-absorbing layer at the top and bottom of the computational domain is used to mitigate the effects of acoustic waves [7,8], which are generated at the interface and propagate outward [41].

Our numerical simulations use uniform grid with periodic boundary conditions in horizontal direction and no-slip boundary condition in vertical direction for the velocity. Gradient-free boundary

TABLE I. The parameters and statistics at $z = 0$ and $t/\tau = 3.0$ of the simulations.

Sr	At	Gr_Δ	M_t	$Re_{\lambda,z}$	$(Re_{\lambda,x} + Re_{\lambda,y})/2$	λ_z/η	$(\lambda_x + \lambda_y)/2\eta$
0.5	0.5	0.745	0.114	65.7	24.7	14.5	9.5
1.0	0.5	0.745	0.153	61.9	22.3	14.1	9.0
2.0	0.5	0.745	0.192	52.7	18.8	13.1	8.2
3.0	0.5	0.745	0.214	45.9	16.8	12.0	7.5

condition for concentration is used in vertical direction. The temperature is kept fixed at the top and bottom boundaries [7,10].

III. THE SIMULATION PARAMETERS AND STATISTICS

The mole fraction of heavy fluid for the binary mixing fluid model is [12]

$$X = \frac{(1 - A_t)c}{1 + A_t - 2A_t c}. \tag{10}$$

We define three spatial averages of a variable φ:

$$\langle \varphi \rangle_{xy}(z, t) = \frac{1}{L_x L_y} \int_0^{L_y} \int_0^{L_x} \varphi(x, y, z, t) dx dy, \tag{11}$$

$$\langle \varphi \rangle_m(t) = \frac{1}{L_x L_y (H_B + H_S)} \int_{-H_S}^{H_B} \int_0^{L_y} \int_0^{L_x} \varphi(x, y, z, t) dx dy dz, \tag{12}$$

$$\langle \varphi \rangle(t) = \frac{1}{2 L_x L_y L_z} \int_{-L_z}^{L_z} \int_0^{L_y} \int_0^{L_x} \varphi(x, y, z, t) dx dy dz, \tag{13}$$

where H_B and H_S are respectively the bubble and spike heights based on the 1% threshold values of mean mole fraction [12,23]. $\langle \cdot \rangle_{xy}$ denotes the horizontal average value. $\langle \cdot \rangle_m$ and $\langle \cdot \rangle$ denote the volume average in the mixing region and volume average in the computational domain, respectively.

The turbulent Mach number, the horizontal and vertical Taylor Reynolds numbers at a given vertical coordinate z are respectively defined as [12,23]

$$M_t(z) = Sr^{1/2} \frac{\sqrt{\langle u_i' u_i' \rangle_{xy}}}{\langle \gamma p/\rho \rangle_{xy}}, \quad Re_{\lambda,i}(z) = Re \frac{\langle \rho \rangle_{xy} \lambda_i [\langle u_i'^2 \rangle_{xy}]^{1/2}}{\mu} \quad \text{(no sum on } i\text{)}, \tag{14}$$

where $u_i' = u_i - \langle u_i \rangle_{xy}$. The horizontal and vertical Taylor microscales are given by $\lambda_i(z) = [\frac{\langle u_i'^2 \rangle_{xy}}{\langle (\partial u_i'/\partial x_i)^2 \rangle_{xy}}]^{1/2}$ (no sum on i).

The parameters and statistics at $z = 0$ and $t/\tau = 3.0$ of the simulations are summarized in Tables I, where the characteristic timescale is defined as $\tau = \sqrt{L_r/(A_t g)}$ [7,23,28]. The mesh Grashoff numbers, $Gr_\Delta = 2 A_t g \Delta^3/(\mu_r/\rho_r)^2 = 2 A_t \Delta^3 Re^2/L_r^3$ [24], are 0.745 and are below 1, which can ensure that the solutions are well resolved in our numerical simulations. In addition, we calculate the Kolmogorov length scale $\eta(z) = [\langle \mu/(Re\rho) \rangle_{xy}^3/\langle \varepsilon/\rho \rangle_{xy}]^{1/4}$, where the local viscous dissipation rate of kinetic energy is $\varepsilon = \sigma_{ij}(\partial u_i/\partial x_j)/Re$. The time evolution of Kolmogorov length scale $\eta(0)/\Delta x$ at $z = 0$ and its profiles as functions of H^* at $t/\tau = 3.0$ for different stratification parameters Sr are shown in Fig. 2. Here, $H^* = z/H_B$ if $z \geqslant 0$, while $H^* = z/H_S$ if $z \leqslant 0$ [12]. We see that $\eta(z)/\Delta x$ is greater than 1.5 for any time, height, and Sr. The Taylor Reynolds numbers and Taylor microscales decrease with the increase of Sr, which is consistent with 2D compressible RT turbulence [12]. The turbulent Mach number M_t increases with an increase of Sr. It is worth noting that the values of M_t are only 0.192 and 0.214 for Sr = 2.0 and 3.0, respectively, which are relatively small.
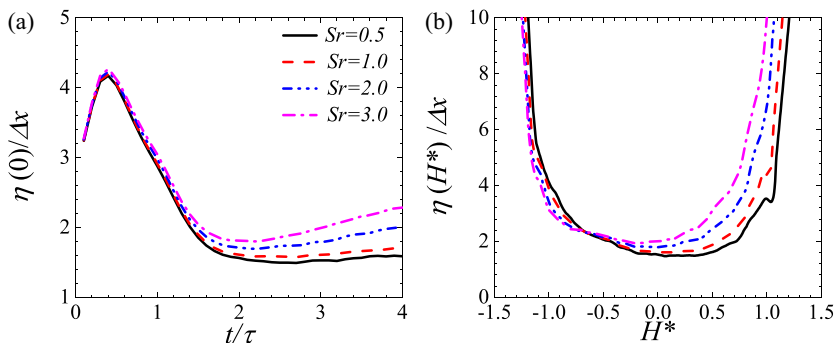
FIG. 2. (a) Time evolution of Kolmogorov length scale $\eta(0)/\Delta x$ at $z = 0$ and (b) mean profiles of Kolmogorov length scale $\eta(H^*)/\Delta x$ as functions of H^* at $t/\tau = 3.0$ for different stratification parameters Sr.

IV. MIXING EVOLUTION

Figure 3 illustrates the contours of mole fraction X for Sr $= 0.5$ at $t/\tau = 1.0, 2.0, 3.0, 4.0$. The development of RT turbulence is clearly observed: the perturbations of different wave numbers grow independently in the beginning; then, the spikes or bubbles compete or merge with each other; and they gradually develop to turbulence in the late stage. At $t/\tau = 1.0$, diffusion and linear growth dominate. The nonlinear effects are very strong, and the structures of bubbles and spikes are complex at $t/\tau = 2.0$. Some statistics become self-similar at $t/\tau \geqslant 2.0$, including the molecular mixing degree (Fig. 8), Kolmogorov length scale (Fig. 2), the turbulent Mach number, Taylor Reynolds numbers, and the mean profiles of mole fraction. The observation is similar to our previous results in compressible 2D RT turbulence at $t/\tau \geqslant 2.0$ and at $A_t = 0.5$ [12].

Mixing heights can be expressed in many different ways. Figure 4 presents the time evolution of bubble and spike heights for three different definitions at different stratification parameters Sr. The bubble and spike heights in Fig. 4(a) are defined as follows [10,35,42]:

$$h_B = 3 \int_0^{L_z} \overline{X}(1 - \overline{X})dz \quad \text{and} \quad h_S = 3 \int_{-L_z}^0 \overline{X}(1 - \overline{X})dz. \tag{15}$$

In Figs. 4(b) and 4(c), $H_{B/S,0.05}$ and $H_{B/S,0.01}$ are the bubble and spike heights based on the 5% and 1% threshold values of mean mole fraction [42–44]. The spike heights decrease slightly with the increase of Sr, and the effects of stratification parameters on bubble heights are different for three different definitions. The stratification parameter has little effect on $H_{B,0.01}$, expect for Sr $= 3.0$. However, the stratification parameter has a relatively weak promoting effect on $H_{B,0.05}$ and significantly promotes the development of h_B. The difference of the influence on differently defined
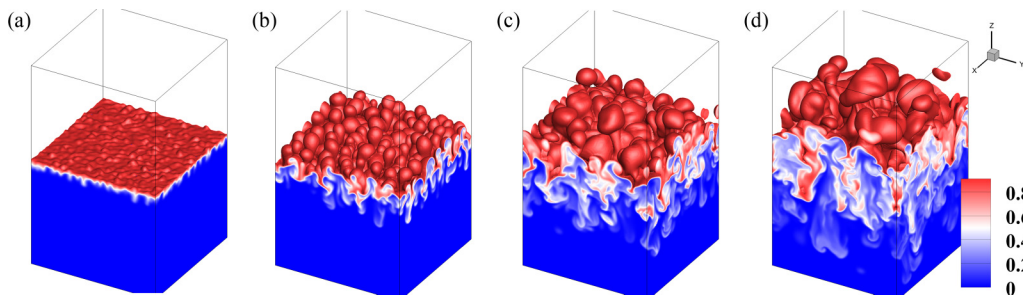

FIG. 3. The contours of mole fraction for Sr $= 0.5$ at (a) $t/\tau = 1.0$, (b) $t/\tau = 2.0$, (c) $t/\tau = 3.0$ and (d) $t/\tau = 4.0$.
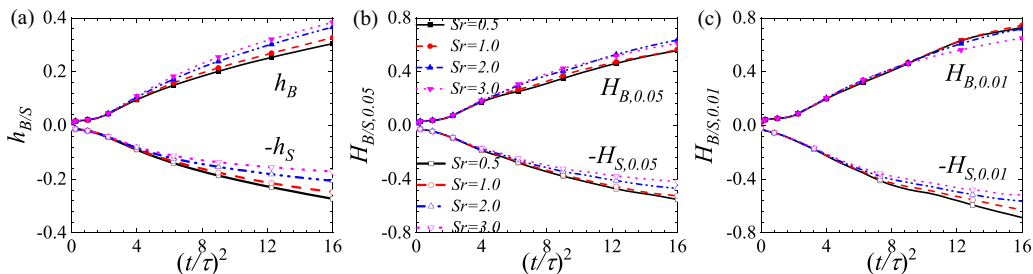
FIG. 4. Time evolution of bubble and spike heights for three different definitions at different stratification parameters Sr: (a) $h_{B/S}$ defining as Eq. (15), (b) $H_{B/S,0.05}$ using the 5% threshold values, and (c) $H_{B/S,0.01}$ using the 1% threshold values.

bubble heights is due to the different shape of bubbles. Figure 5 shows the contours of mole fraction for different stratification parameters at $t/\tau = 3.0$. We can see that the bubbles become bigger with the increase of Sr. In other words, assuming that the top of the bubble is at the same height for different Sr, there are more light fluids at the same distance from the top at large Sr. Therefore, the bubble height with big bubble at large Sr is greater than that at small Sr. In addition, the nearly proportional relation between differently defined bubble heights in incompressible RT turbulence is not observed in compressible flow [42–44].

Figure 6 shows the mean density profile with height z at Sr = 2.0, 3.0 and different times. For the stratification parameter Sr = 3.0, we can't see the density difference at the top of the bubble in the density profile, and there is basically no inverse gradient for density profile at $t/\tau \geqslant 2.5$. However, mixing can continue to develop until the end of the simulations. The mixing heights and density profiles are significantly different from the incompressible density stratified RT turbulence [45–47]. There are three reasons for the growth of bubble height without density difference of the mean density profile at the top of the bubble: the first is that the density in the bubble is lower than that outside the bubble in the local range of the bubble top (this effect will be weaken with the decrease of density outside the bubble until it disappears); the second is upward inertia of bubble; the third is the strong expansion and compression motions, which convert the internal energy to kinetic energy (Fig. 11), making the light fluid continue to move upward. The first two reasons also exist in incompressible stratified RT turbulence, and the last one is unique in compressible RT turbulence. The expansion and compression motions increase with the increase of Sr, and they play a more significant role compared with the initial density stratification in the developing of RT instability at large Sr and Atwood numbers. In addition, we notice that the density outside the bubble
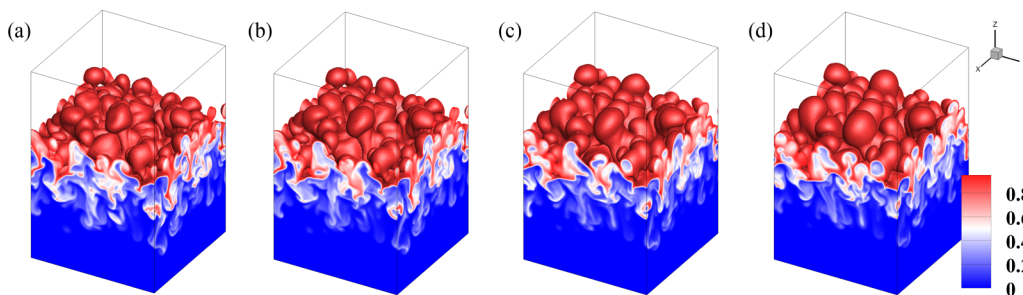

FIG. 5. The contours of mole fraction for different stratification parameters at $t/\tau = 3.0$ and different stratification parameters Sr: (a) Sr = 0.5, (b) Sr = 1.0, (c) Sr = 2.0, and (d) Sr = 3.0.

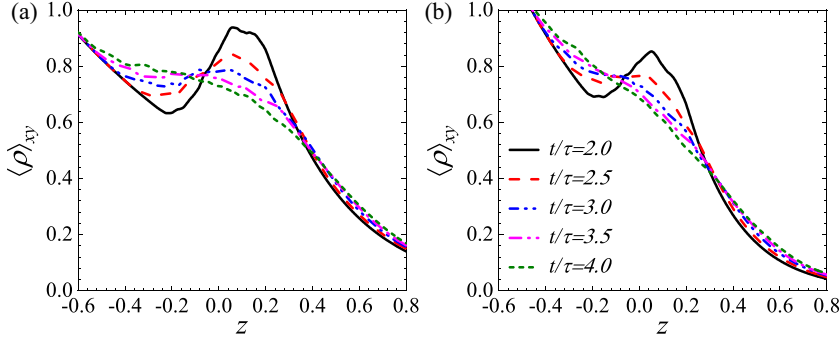FIG. 6. The mean density profiles at different times and stratification parameters Sr: (a) Sr = 2.0 and (b) Sr = 3.0.

increases with time because it is compressed [12]. The similar density profile occurs for Sr = 2.0 at $t/\tau \geqslant 3.0$.

According to the different definitions of bubble and spike heights, we can define the following different ratios of bubble heights to spike heights:

$$\beta_h = \frac{h_B}{h_S}, \quad \beta_{0.05} = \frac{H_{B,0.05}}{H_{S,0.05}}, \quad \text{and} \quad \beta_{0.01} = \frac{H_{B,0.01}}{H_{S,0.01}}. \tag{16}$$

Figure 7 displays the time evolution of three ratios for different stratification parameters Sr. These ratios increase with the increase of Sr, which is consistent with 2D compressible RT turbulence [12]. $\beta_{0.01}$ is least affected by Sr, while β_h is the most affected by Sr. The difference between three ratios is mainly due to the different effects of the stratification parameters on the three bubble heights. It is worth noting that β_h develops linearly with time at $t/\tau > 2.0$. By fitting the curve at $2.0 \leqslant t/\tau \leqslant 4.0$, we find that the 2/3 power of the slope is proportional to Sr, i.e., $k_s^{2/3} \sim$ Sr, where k_s is the slope of β_h.

For compressible RT turbulence with isothermal initial equilibrium, the density of light or heavy fluid is exponentially distributed, so it is difficult to calculate the mixed mass given in incompressible RT turbulence [27,48]. However, the molar mass of light or heavy fluid is constant in our simulations. Therefore, the normalized mixed molar mass Ψ and molecular mixing degree Θ are defined as [10,27,48,49]

$$\Psi = \frac{\langle Mc(1-c)\rangle_m}{\langle\langle M\rangle_{xy}\langle c\rangle_{xy}\langle 1-c\rangle_{xy}\rangle_m} \quad \text{and} \quad \Theta = \frac{\langle X(1-X)\rangle_m}{\langle\langle X\rangle_{xy}\langle 1-X\rangle_{xy}\rangle_m}, \tag{17}$$
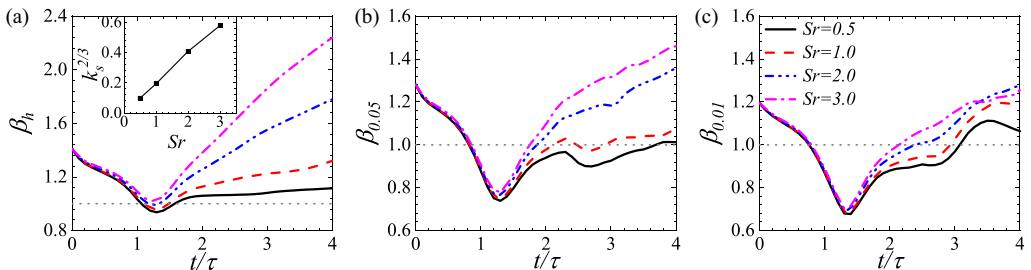

FIG. 7. Time evolution of three ratios of bubble height to spike height defining as Eq. (16) at different stratification parameters Sr: (a) β_h, (b) $\beta_{0.05}$, and (c) $\beta_{0.01}$.
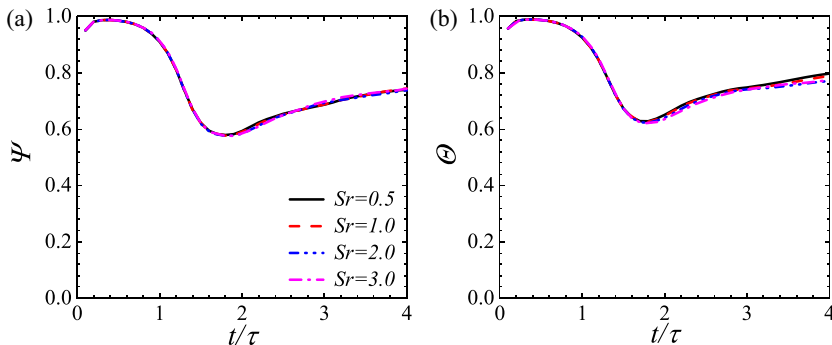
FIG. 8. Time evolution of (a) the normalized mixed molar mass Ψ and (b) the molecular mixing degree Θ at different stratification parameters Sr.

where, M is the molar mass of the mixed fluid, and $1/M = c/M_H + (1-c)/M_L$. Figure 8 presents the time evolution of Ψ and Θ for different stratification parameters Sr. The stratification parameter has no obvious effect on Ψ and Θ, which is consistent with 2D compressible RT turbulence [12]. Ψ and Θ increase slowly at $t/\tau > 2.0$ and gradually approach constants about 0.75 and 0.8, respectively. They are close to the results of incompressible RT turbulence [27,48].

Considering that the bubble is bigger at large Sr, which has an impact on molecular mixing, we further study the molecular mixing degree at different vertical heights. Figure 9 shows the mean profile of molecular mixing degree $\Theta_{xy} = \frac{\langle X(1-X)\rangle_{xy}}{\langle X\rangle_{xy}\langle 1-X\rangle_{xy}}$ as functions of H^* at different Sr. Stratification parameter promotes the molecular mixing at $-1 < H^* < 0.5$, but suppresses the molecular mixing at $0.5 < H^* < 1.0$. This is because the large bubbles and simple vortex structures reduce the contact areas between light fluid and heavy fluid, which leads to less mixing of two fluids at $0.5 < H^* < 1.0$. This phenomenon may be more obvious at higher Atwood numbers and stratification parameters.
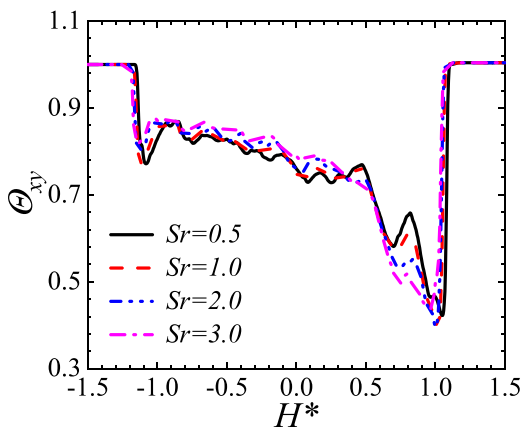

FIG. 9. The mean profiles of molecular mixing degree Θ_{xy} as functions of H^* at $t/\tau = 3.0$ for different stratification parameters Sr.
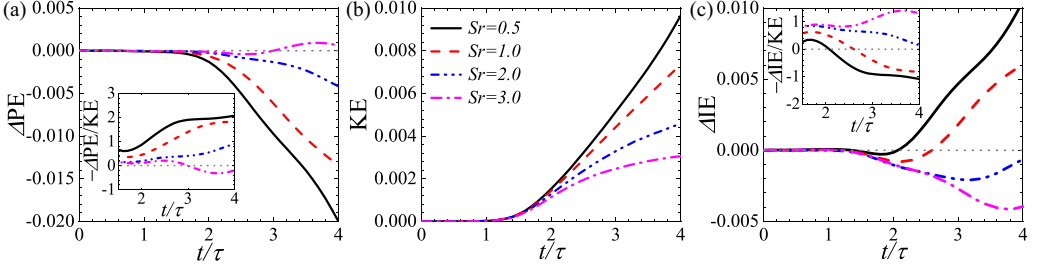
FIG. 10. Time evolution of (a) potential energy variation $\Delta\mathrm{PE} = \mathrm{PE} - \mathrm{PE}_0$, (b) kinetic energy, and (c) internal energy variation $\Delta\mathrm{IE} = \mathrm{IE} - \mathrm{IE}_0$ at different stratification parameters, where PE_0 and IE_0 are the potential energy and internal energy at $t/\tau = 0$. The ratios $-\Delta\mathrm{PE}/\mathrm{KE}$ and $-\Delta\mathrm{IE}/\mathrm{KE}$ are plotted in the inset.

V. ENERGY TRANSFER

A. Conversion between different forms of energy

There are three different forms of energy in compressible RT turbulence: potential energy (PE), kinetic energy (KE), and internal energy (IE). Potential energy is continuously converted to kinetic energy with a conversion efficiency of about 50% in three-dimensional incompressible RT turbulence [25,26]. The work done by pressure and viscosity in compressible fluid can lead to the conversion of kinetic energy and internal energy [28,34].

The kinetic energy is governed by [12,28]

$$\frac{\partial}{\partial t}\left(\frac{1}{2}\rho u_i^2\right) + \frac{\partial}{\partial x_j}\left(\frac{1}{2}\rho u_i^2 u_j + \frac{1}{\mathrm{Sr}}pu_j - \frac{1}{\mathrm{Re}}u_i\sigma_{ij}\right) = \frac{p}{\mathrm{Sr}}\theta - \frac{\sigma_{ij}}{\mathrm{Re}}\frac{\partial u_i}{\partial x_j} - \rho u_3. \tag{18}$$

Taking the volume average over the computational domain and using boundary conditions, we obtain

$$\frac{d\mathrm{KE}}{dt} = I - \Phi - \varepsilon, \tag{19}$$

where $\mathrm{KE} = \langle\frac{1}{2}\rho u_i u_i\rangle$ is the kinetic energy, $I = -\langle\rho u_3\rangle$ is the energy transfer rate from potential energy to kinetic energy, $\varepsilon = \langle\sigma_{ij}(\partial u_i/\partial x_j)\rangle/\mathrm{Re}$ is the viscous dissipation and $\Phi = -\langle p\theta\rangle/\mathrm{Sr}$ is the pressure-dilatation work. $p\theta/\mathrm{Sr}$ is positive in the expansion region and negative in the compression region, which indicates the energy exchanges between internal energy and kinetic energy caused by pressure work [12,34,50]. The volume average of internal energy is governed by [12]

$$\frac{d\mathrm{IE}}{dt} = \mathrm{Sr}(\gamma_r - 1)(\Phi + \varepsilon), \tag{20}$$

where $\mathrm{IE} = \langle\rho e\rangle$ is the internal energy.

In Fig. 10, we show the time evolution of potential energy variation $\Delta\mathrm{PE} = \mathrm{PE} - \mathrm{PE}_0$, kinetic energy and internal energy variation $\Delta\mathrm{IE} = \mathrm{IE} - \mathrm{IE}_0$ at different stratification parameters, where PE_0 and IE_0 are the potential energy and internal energy at $t/\tau = 0$. The ratios $-\Delta\mathrm{PE}/\mathrm{KE}$ and $-\Delta\mathrm{IE}/\mathrm{KE}$ are plotted in the inset. The kinetic energy increases with time and decreases with the increase of Sr, because density stratification weakens velocity fluctuations and the average density is small at large Sr [12]. The potential energy variation $\Delta\mathrm{PE}$ is negative and the absolute value increases with the increase of time and Sr at $\mathrm{Sr} \leqslant 2.0$. The potential energy is constantly converted to kinetic energy, but density stratification weakens this process. However, $\Delta\mathrm{PE}$ has a positive value at $t/\tau > 3.0$ for $\mathrm{Sr} = 3.0$, which is obviously different from the incompressible RT turbulence and the compressible RT turbulence at $\mathrm{Sr} \leqslant 2.0$. In Fig. 10(c), $\Delta\mathrm{IE}$ is negative for $\mathrm{Sr} \geqslant 2.0$. $\Delta\mathrm{IE}$ is negative at the beginning and then becomes positive for $\mathrm{Sr} \leqslant 1.0$.
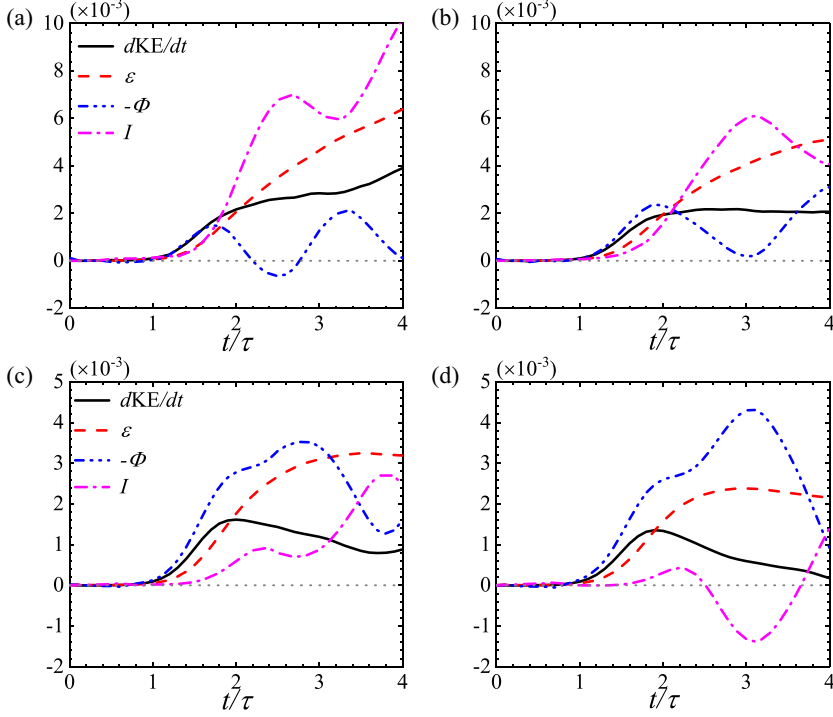
FIG. 11. Time evolution of the terms in the equation of kinetic energy (19) for different stratification parameters (a) Sr = 0.5, (b) Sr = 1.0, (c) Sr = 2.0, and (d) Sr = 3.0.

In the later stage, $-\Delta$PE/KE gradually increases to 2 or 1.8, $-\Delta$IE/KE decreases to -1 or -0.8 at Sr = 0.5 or 1.0, respectively. This observation indicates that the kinetic energy mainly comes from the potential energy. About 50% of the transformed potential energy is lost in the form of kinetic energy, and about 50% of the transformed potential energy is lost in the form of heat, which is consistent with the 3D incompressible RT turbulence [25,26]. At Sr = 2.0, $-\Delta$PE/KE increases from 0.2 to 0.9 and $-\Delta$IE/KE decreases from 0.8 to 0.1. The kinetic energy mainly comes from internal energy at the beginning and gradually tends to come from potential energy with the increase of time. At Sr = 3.0, $-\Delta$PE/KE is very small and becomes negative, and $-\Delta$IE/KE exceeds 1.0 at $t/\tau \geqslant 3.0$. This observation indicates that most of internal energy is first converted to kinetic energy, and then kinetic energy is converted to potential energy. This process increases the kinetic energy of the flow field and promotes the further development of the mixing height (Fig. 4) at large Sr. In addition, potential energy is transformed into kinetic energy only in the vertical direction, while the horizontal and vertical components of pressure dilatation act as source of kinetic energy at large scales [14], which may be one of the reasons for the big bubbles at large Sr.

Figure 11 presents the time evolution of each term in Eq. (19) for Sr = 0.5, 1.0, 2.0, 3.0. dKE/dt is always positive, indicating that kinetic energy increases with time, which is consistent with Fig. 10. dKE/dt increases at $t/\tau < 2.0$ and has different trends for different Sr at $t/\tau \geqslant 2.0$. The viscous dissipation ε is always positive, which converts kinetic energy to internal energy. It maintains a relatively large value and decreases with the increase of Sr. Both ε and Φ lead to the changes of average kinetic energy and internal energy.

The energy transfer rate I is positive for Sr $\leqslant$ 2.0, which indicates that potential energy is converted to kinetic energy all the time. Note that I is negative at $2.4 < t/\tau < 3.6$ for Sr = 3.0, which is related to the fact that the mean density profiles have no inverse gradient for $t/\tau \geqslant 2.5$ (Fig. 6). This observation indicates that kinetic energy is converted to potential energy. This
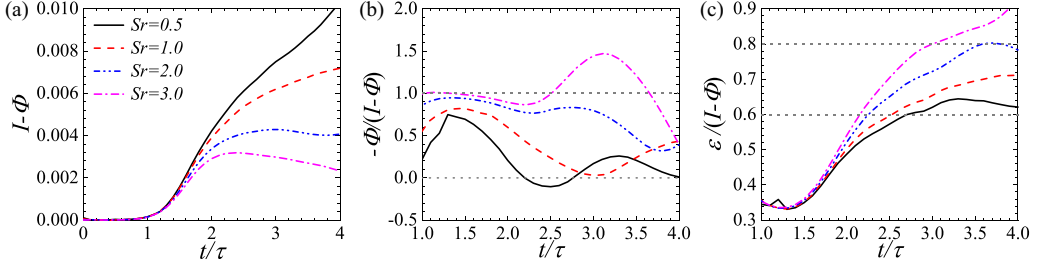
FIG. 12. Time evolution of (a) total production of kinetic energy $I - \Phi$, (b) the ratios of the pressure-dilatation work to the total production $-\Phi/(I - \Phi)$, and (c) the viscous dissipation to total production $\varepsilon/(I - \Phi)$ for different stratification parameters Sr.

phenomenon exists in the case of large Atwood numbers and large stratification parameters. I decreases with the increase of Sr, which is caused by the initial density stratification. In contrast to I, the pressure-dilatation work $-\Phi$ increases with the increase of Sr. The pressure-dilatation work fluctuates around 0 at very small Sr [12,14]. As the stratification parameter increases, the fluctuation weakens and the pressure-dilatation work $-\Phi$ gradually tends to be positive value. I or $-\Phi$ may be a negative value at some parameters and times. However, $I - \Phi$ is always positive as shown in Fig. 12. Thus, $I - \Phi$ can be regraded as the source of kinetic energy.

Figure 12 presents the time evolution of total production of kinetic energy $I - \Phi$, the ratios of the pressure-dilatation work to the total production $-\Phi/(I - \Phi)$ and the viscous dissipation to total production $\varepsilon/(I - \Phi)$. The total production of kinetic energy $I - \Phi$ decreases with the increase of Sr, which is consistent with 2D compressible RT turbulence [12]. Overall, the ratio $-\Phi/(I - \Phi)$ increases with the increase of Sr. $-\Phi/(I - \Phi)$ at Sr = 0.5 is similar with 2D compressible RT turbulence at Sr = 0.1. It is essentially less than 0.5 at $t/\tau \geqslant 2.0$ for Sr = 1.0 in the present study, but 85% of the kinetic energy is from the pressure-dilatation work at Sr = 1.0 in 2D compressible RT turbulence [12]. The observation indicates that the effect of pressure-dilatation work on kinetic energy generation is weaker than that in 2D compressible RT turbulence. At large stratification parameter Sr = 3.0, $-\Phi/(I - \Phi)$ fluctuates around 1, and reaches a maximum value about 1.5 at $t/\tau = 3.0$, because of negative I. The ratio $\varepsilon/(I - \Phi)$ increases with the increase of Sr, which is also consistent with 2D RT turbulence [12]. The large $\varepsilon/(I - \Phi)$ means that the growth of kinetic energy is relatively slow at large Sr. $\varepsilon/(I - \Phi)$ reaches 60% for Sr = 0.5 and exceeds 80% for Sr = 3.0 at $t/\tau \geqslant 3.0$. These values are much greater than 0.1 in 2D compressible RT turbulence [12]. Although pressure-dilatation work is weaker in converting internal energy to kinetic energy, the viscous dissipation is stronger in converting kinetic energy to internal energy, as compared to the situation of 2D compressible RT turbulence.

Let us make a brief summary of the main results of this section: (i) The kinetic energy comes from two sources: the conversion of potential energy and conversion of internal energy through pressure-dilatation work. Kinetic energy mainly comes from potential energy at small Sr (Sr $\leqslant 1.0$) and internal energy at large Sr (Sr $\geqslant 2.0$), which is the result of the combined effect of initial density stratification and expansion-compression motions. (ii) For large stratification parameter Sr = 3.0, internal energy is first converted to kinetic energy, and then kinetic energy is converted to potential energy. This process may promote the further development of bubble height and produce the big bubbles. (iii) The effects of Sr on the $-\Phi$ and I in 3D compressible RT turbulence are consistent with 2D RT turbulence. However, compared with 2D RT turbulence, the contribution of pressure-dilatation work $-\Phi$ to kinetic energy generation is significantly smaller at a given Sr in 3D flow.

B. The scale-to-scale transfer of kinetic energy

A filtering technique can be used to analyze interscale transfer of kinetic energy in compressible RT turbulence [14,28]. For a given field f, the filtered field $\bar{f}$ is

$$\bar{f}(x) \equiv \int d^3 r G_l(r) f(x+r), \tag{21}$$

where $G_l(\boldsymbol{r}) \equiv l^{-3} G(\boldsymbol{r}/l)$ is the filter function, $G(r)$ is a normalized window function, and l represents the filter width. The Favre filtered field is defined as $\tilde{f} \equiv \overline{\rho f}/\bar{\rho}$. A top-hat filter is used and calculated in one dimension by [51]

$$\bar{f}_i = \frac{1}{4n}\left(f_{i-n} + 2 \sum_{j=i-n+1}^{i+n-1} f_j + f_{i+n}\right), \tag{22}$$

where the filter width is $l = 2n\Delta x$.

The Favre filtered equation for the average of the large-scale kinetic energy can be derived as [14,28,52,53]

$$\frac{\partial}{\partial t}\left\langle \frac{1}{2}\bar{\rho}\tilde{u}_i^2 \right\rangle + \langle J_l \rangle = \langle I_l \rangle - \langle \Phi_l \rangle - \langle \Pi_l \rangle - \langle \varepsilon_l \rangle, \tag{23}$$

where J_l is the space transport of large-scale kinetic energy, I_l is the energy injected by gravity, Φ_l is the large-scale pressure-dilatation term, Π_l is the SGS kinetic energy flux, and ε_l is the viscous dissipation term. They are defined as

$$J_l \equiv \frac{\partial}{\partial x_j}\left(\frac{1}{2}\bar{\rho}\tilde{u}_i^2 \tilde{u}_j + \frac{1}{\mathrm{Sr}}\bar{p}\tilde{u}_j + \bar{\rho}\tilde{\tau}_{ij}\tilde{u}_i - \frac{\tilde{u}_i \bar{\sigma}_{ij}}{\mathrm{Re}} \right), \quad I_l \equiv -\bar{\rho}\tilde{u}_3, \quad \Phi_l \equiv -\frac{\bar{p}}{\mathrm{Sr}}\frac{\partial \tilde{u}_i}{\partial x_i},$$

$$\Pi_l \equiv -\bar{\rho}\tilde{\tau}_{ij}\frac{\partial \tilde{u}_i}{\partial x_j} = -\bar{\rho}\tilde{\tau}_{ij}\tilde{S}_{ij}, \quad \varepsilon_l \equiv \frac{\bar{\sigma}_{ij}}{\mathrm{Re}}\frac{\partial \tilde{u}_i}{\partial x_j}, \tag{24}$$

where the SGS stress is $\bar{\rho}\tilde{\tau}_{ij} = \bar{\rho}(\widetilde{u_i u_j} - \tilde{u}_i \tilde{u}_j)$, and the filtered strain-rate tensor is $\tilde{S}_{ij} = (\partial \tilde{u}_i/\partial x_j + \partial \tilde{u}_j/\partial x_i)/2$.

Figure 13 presents the average of kinetic energy transfer terms on the right-hand side of Eq. (23) for stratification parameters $\mathrm{Sr} = 0.5, 1.0, 2.0, 3.0$ at $t/\tau = 3.0$. For $\mathrm{Sr} \leqslant 2$, the kinetic energy is mainly injected from PE at the largest scale [14,29], so I_l is almost constant and is nearly independent of l. But I_l is approximately a negative constant at all scales for $\mathrm{Sr} = 3$ because of negative I [Fig. 11(d)]. This observation indicates that the conversion of kinetic energy to potential energy also exists at large scales. The observations are different with previous studies on compressible RT turbulence [14,28], which can be attributed to the facts that the stratification parameter Sr is not large enough for initial isothermal stratification [28] and ρ is constant for initial isopycnic stratification [14].

The SGS kinetic energy flux $\langle \Pi_l \rangle$ and the viscous dissipation term $\langle \varepsilon_l \rangle$ are basically positive and decrease with the increase of Sr, which are related to the generation $I - \Phi$ and dissipation of kinetic energy. $\langle \varepsilon_l \rangle$ is strong at small scales and can be negligible at large scales [14,28,29,34]. $\langle \varepsilon_l \rangle$ can be well normalized with ε for different Sr as shown in Fig. 14. $\langle \varepsilon_l \rangle/\varepsilon$ exhibits a scaling behavior of $(l/\Delta x)^{-3.5}$ at large scales $l/\Delta x \geqslant 50$. Zhao and Aluie also found that the decay of kinetic energy dissipation is faster than l^{-2} at large scales for $A_t = 0.8$ in RT turbulence [30]. This decay of viscous dissipation with scale is much greater than $(l/\Delta x)^{-1.5}$ in forced anisotropic turbulence (FAT) [54] and in homogeneous isotropic turbulence (HIT) [34], suggesting that the correlation between small scales and large scales is weaker, and the effect of viscosity on large-scale kinetic energy transfer is much smaller in RT turbulence, as compared to the situations of FAT and HIT. It is worth noting that the large-scale pressure-dilatation term $\langle \Phi_l \rangle$ is close to $\langle I_l \rangle$ at large scales about $l/\Delta x > 100$, indicating the $\frac{\partial}{\partial t}\langle \frac{1}{2}\bar{\rho}\tilde{u}_i^2 \rangle$ is small at large scales. This observation is consistent with the studies for initial isopycnic stratification of Zhao et al. [14].
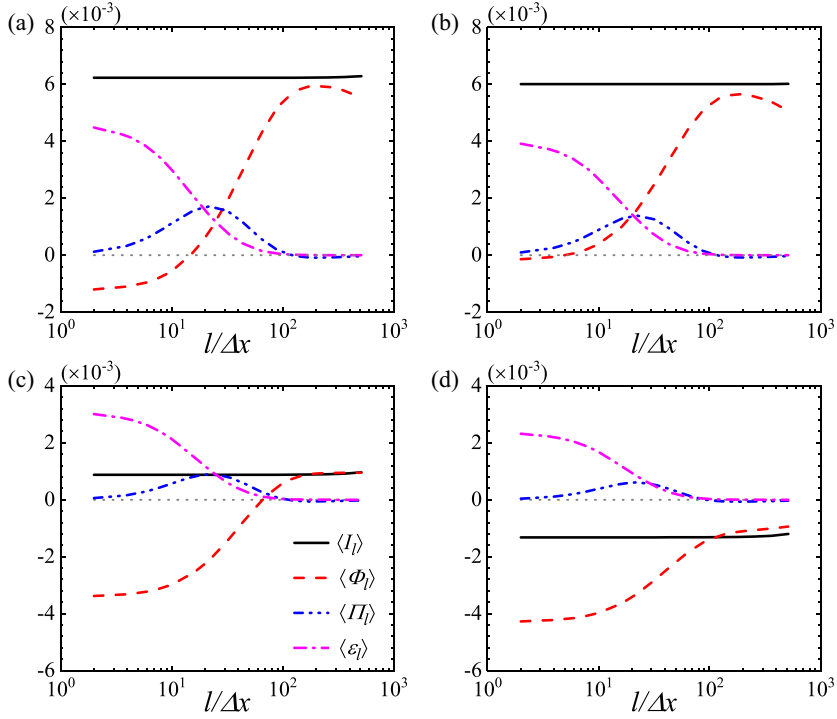
FIG. 13. The average of the terms in filtered equation of kinetic energy (23) at $t/\tau = 3.0$ for different stratification parameters (a) Sr = 0.5, (b) Sr = 1.0, (c) Sr = 2.0, and (d) Sr = 3.0.
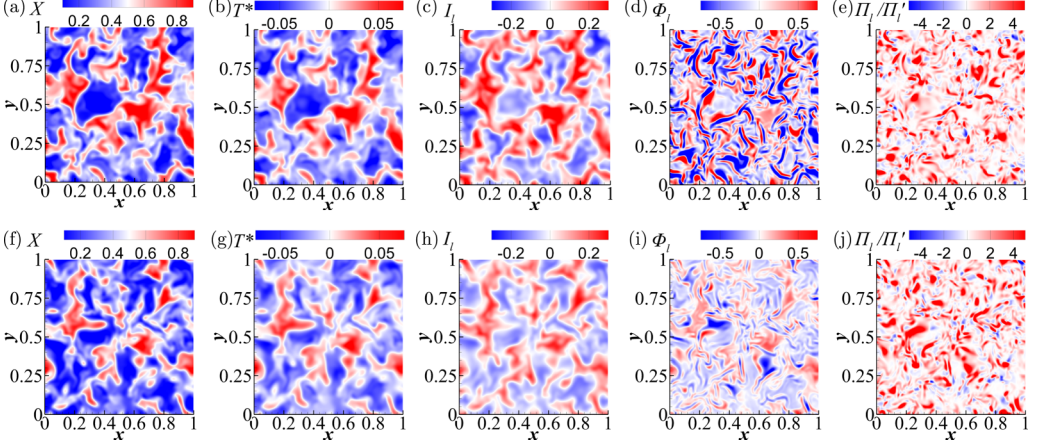
Figure 15 presents the contours of mole fraction X, normalized temperature $T^* = (T - T_0)/\text{Sr}$, energy injected by gravity I_l, large-scale pressure-dilatation Φ_l, SGS flux of kinetic energy Π_l/Π_l' at filter width $l/\Delta x = 12$ for Sr = 1.0, 3.0 at $z = 0$ and $t/\tau = 3.0$. The heavy fluid moves downward, the potential energy is converted to kinetic energy, and the temperature increases. The upward
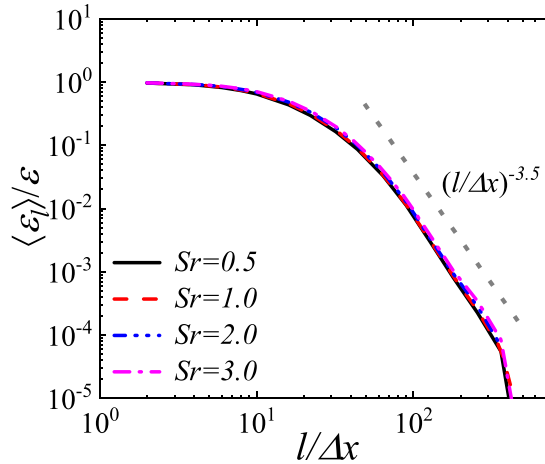
FIG. 14. Normalized average of the viscous dissipation term $\varepsilon_l/\varepsilon$ at $t/\tau = 3.0$ for stratification parameters Sr = 0.5, 1.0, 2.0, 3.0.

FIG. 15. The contours of mole fraction X, normalized temperature $T^* = (T - T_0)/\text{Sr}$, energy injected by gravity I_l, large-scale pressure-dilatation Φ_l, SGS flux Π_l/Π_l' at filter width $l/\Delta x = 12$ for $\text{Sr} = 1.0 (a - e)$, and $\text{Sr} = 3.0 (f - j)$ at $z = 0$ and $t/\tau = 3.0$.

moving light fluid causes the conversion of kinetic energy to potential energy, and the temperature decreases. At a small stratification parameter, the strong positive and negative pressure-dilatation are distributed adjacent to each other in the interface of light and heavy fluids, owing to the diffusive mixing of the two unequal-density species [12,23]. And its spatial average value is nearly zero. The downward moving heavy fluid tends to be compressed, and the upward moving light fluid tends to exist in the state of dilatation [12]. Therefore, Φ_l is generally positive in heavy fluid regions and is generally negative in the light fluid. As Sr increases, the pressure-dilatation is weakened in the interface and is enhanced inside light or heavy fluid, owing to the strong expansion and compression motions at large Sr. The conversion between internal energy and kinetic energy becomes stronger at large Sr. The positive SGS flux of kinetic energy is much larger than the negative SGS flux, which is irregularly distributed in the flow field.

C. SGS kinetic energy flux

Figure 16 shows the normalized average of the SGS flux of kinetic energy at different stratification parameters Sr. $\langle \Pi_{\text{max}} \rangle$ is the maximum value of average SGS flux, for example $\langle \Pi_{\text{max}} \rangle$ is the $\langle \Pi_l \rangle$ at filter width $l/\Delta x = 22$ for $t/\tau = 3.0$. The normalized average values of SGS kinetic energy
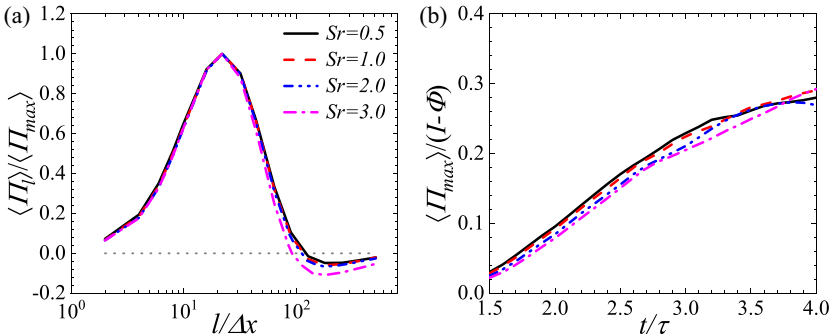

FIG. 16. (a) Normalized average of the SGS flux of kinetic energy $\langle \Pi_l \rangle/\langle \Pi_{\text{max}} \rangle$ at $t/\tau = 3.0$ and (b) the time evolution of $\langle \Pi_{\text{max}} \rangle/(I - \Phi)$ at stratification parameters $\text{Sr} = 0.5, 1.0, 2.0, 3.0$.
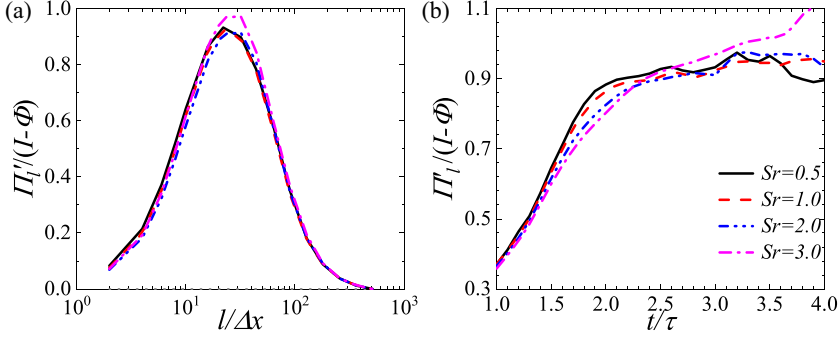
FIG. 17. (a) Normalized r.m.s. values of SGS flux $\Pi_l'/(I - \Phi)$ at $t/\tau = 3.0$ and (b) the time evolution of the r.m.s. values of SGS flux at filter width $l/\Delta x = 22$ at stratification parameters $Sr = 0.5, 1.0, 2.0, 3.0$.

flux $\langle \Pi_l \rangle / \langle \Pi_{\max} \rangle$ nearly collapse onto the same curve at $t/\tau = 3.0$, especially at middle scales, indicating that $\langle \Pi_l \rangle$ is not only self-similar in time [14], but also similar for different Sr. Although the sources of large-scale kinetic energy are different, the kinetic energy cascade is similar. $I - \Phi$ as the source of kinetic energy can be used to normalize the SGS flux. The maximum values of normalized SGS flux $\langle \Pi_{\max} \rangle / (I - \Phi)$ basically appear at the same filter width for different Sr at a given time. They vary approximately linearly with time at $t/\tau \leqslant 3.0$, which decrease slightly as Sr increases. Note that upscale cascade of kinetic energy exists at large scales $l/\Delta x > 100$, and becomes stronger with the increase of Sr, owing to the strong negative SGS flux at large Sr shown in Fig. 18, but it is much weaker than downscale cascade at middle scales. The scales of upscale cascade increase with the development of RT turbulence, which is consistent with previous studies [14,28].

The normalized root-mean-square (r.m.s.) value of SGS flux is defined as $\Pi_l' = \sqrt{\langle (\Pi_l - \langle \Pi_l \rangle_{xy})^2 \rangle}$. We depict $\Pi_l'/(I - \Phi)$ at $t/\tau = 3.0$ and $\Pi_l'/(I - \Phi)$ at filter width $l/\Delta x = 22$ with time in Fig. 17. The behavior of r.m.s. value of SGS flux $\Pi_l'/(I - \Phi)$ is similar to that of its average value, which is basically independent of Sr and has the maximum value at filter width $l/\Delta x = 22$ for $t/\tau = 3.0$. $\Pi_l'/(I - \Phi)$ at filter width $l/\Delta x = 22$ increases with time at $t/\tau \leqslant 2.0$ and gradually approaches a constant about $0.9 \sim 0.98$ for $Sr \leqslant 2.0$. At $Sr = 3.0$, $\Pi_l'/(I - \Phi)$ reaches 0.9 at $t/\tau = 2.4$ and continues to increase slowly.
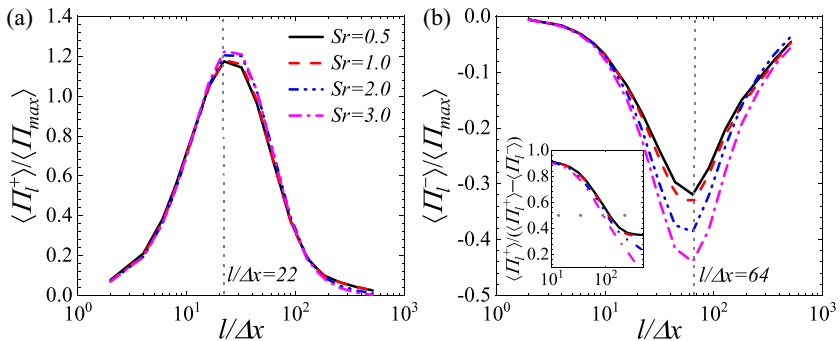

FIG. 18. Normalized average of the positive and negative components of SGS flux at $t/\tau = 3.0$ for stratification parameters $Sr = 0.5, 1.0, 2.0, 3.0$: (a) $\langle \Pi_l^+ \rangle / \langle \Pi_{\max} \rangle$ and (b) $\langle \Pi_l^- \rangle / \langle \Pi_{\max} \rangle$. In the inset, the ratio $\langle \Pi_l^+ \rangle / (\langle \Pi_l^+ \rangle - \langle \Pi_l^- \rangle)$ is depicted.

We decompose the SGS flux Π_l into a positive component Π_l^+ and a negative component Π_l^-:

$$\Pi_l^+ = \tfrac{1}{2}(\Pi_l + |\Pi_l|), \qquad \Pi_l^- = \tfrac{1}{2}(\Pi_l - |\Pi_l|). \tag{25}$$

Figure 18 shows the normalized average of the positive and negative components of SGS flux for different stratification parameters Sr at $t/\tau = 3.0$. The stratification parameter has little effect on positive component $\langle\Pi_l^+\rangle/\langle\Pi_{\max}\rangle$ at middle scales. The magnitude of negative component $\langle\Pi_l^-\rangle/\langle\Pi_{\max}\rangle$ increases with the increase of Sr, demonstrating that flow compressibility promotes upscale cascade of kinetic energy from small scales to large scales. Because the reverse SGS flux is much weaker than the direct SGS flux at small and middle scales, the SGS flux is basically independent of Sr. In addition, we notice that the largest positive component occurs at filter width $l/\Delta x = 22$, which is consistent with the SGS flux shown in Fig. 16. However, the maximum absolute value of negative component is at filter width $l/\Delta x = 64$, which is larger than $l/\Delta x = 22$ of positive component, indicating that reverse SGS flux of kinetic energy tends to appear at the larger scales than direct SGS flux. We plot the ratio $\langle\Pi_l^+\rangle/(\langle\Pi_l^+\rangle - \langle\Pi_l^-\rangle)$ in the inset, which can represent the relative intensity of direct SGS flux and reverse SGS flux of kinetic energy. $\langle\Pi_l^+\rangle/(\langle\Pi_l^+\rangle - \langle\Pi_l^-\rangle)$ decreases with the increase of filter width $l/\Delta x$ and is greater than 0.5 at $l/\Delta x < 100$, demonstrating a net downscale cascade of kinetic energy at small and middle scales. However, it is less than 0.5 and decreases with the increase of Sr at $l/\Delta x > 100$. This observation indicates the upscale cascade at large scales and is consistent with Fig. 16.

D. Effect of velocity divergence on SGS flux of kinetic energy

To study the effect of velocity divergence on SGS flux of kinetic energy, we consider the following conditional average of the positive and negative components of SGS flux of kinetic energy: $\langle\Pi_l^+ \mid \theta_l > 0\rangle_m/(I - \Phi)$, $\langle\Pi_l^+ \mid \theta_l < 0\rangle_m/(I - \Phi)$, $\langle\Pi_l^- \mid \theta_l > 0\rangle_m/(I - \Phi)$, and $\langle\Pi_l^- \mid \theta_l < 0\rangle_m/(I - \Phi)$. We plot them for different stratification parameters Sr at $t/\tau = 3.0$ in Fig. 19. The trends of these curves with filter width are similar to the normalized average of the positive and negative components shown in Fig. 18. We observe that $\langle\Pi_l^+ \mid \theta_l < 0\rangle_m/(I - \Phi)$ is greater than $\langle\Pi_l^+ \mid \theta_l > 0\rangle_m/(I - \Phi)$. However, $\langle\Pi_l^- \mid \theta_l < 0\rangle_m/(I - \Phi)$ is less than $\langle\Pi_l^- \mid \theta_l > 0\rangle_m/(I - \Phi)$. Therefore, the compression motions ($\theta_l < 0$) enhance direct SGS flux of kinetic energy from large scales to small scales, while the expansion motions ($\theta_l > 0$) strengthen the reverse SGS flux of kinetic energy from small scales to large scales. This effect is opposite to the effect of velocity divergence on the baropycnal work. The expansion motions enhance the positive baropycnal work, while the compression motions strengthen the negative baropycnal work [28].

We observe that the conditional average of the positive component $\langle\Pi_l^+ \mid \theta_l > 0\rangle_m/(I - \Phi)$ and $\langle\Pi_l^+ \mid \theta_l < 0\rangle_m/(I - \Phi)$ are basically independent of Sr. However, the magnitude of the conditional average of the negative component $\langle\Pi_l^- \mid \theta_l > 0\rangle_m/(I - \Phi)$ increases with the increase of Sr, which is consistent with the normalized average of the negative component of SGS flux. In addition, at large scales $l/\Delta x \geqslant 100$, the absolute value of $\langle\Pi_l^- \mid \theta_l > 0\rangle_m/(I - \Phi)$ is large than $\langle\Pi_l^+ \mid \theta_l > 0\rangle_m/(I - \Phi)$, while the conditional average of negative component is less than positive component for $\theta_l < 0$. This observation indicates that the net upscale cascade at large scales only exists in the expansion regions, owing to the strong reverse SGS flux of kinetic energy from small scales to large scales.

Figure 20 depicts the isosurfaces of SGS flux of kinetic energy at $\Pi_l/\Pi_l' = 2.0$ for the filter width $l/\Delta x = 22$ at $t/\tau = 3.0$, for different stratification parameters Sr = 0.5, 1.0, 2.0, 3.0. The isosurfaces are colored based on the normalized filtered velocity divergence θ_l/θ_l'. We see that the structures of isosurfaces $\Pi_l/\Pi_l' = 2.0$ are similar for different Sr. The positive θ_l/θ_l' is mainly distributed in the upper half of the mixing layer, while the negative θ_l/θ_l' is mainly distributed in the lower part. This is related to the expansion motions of upward moving light fluid and compression motions of downward moving heavy fluid [12]. It is worth noting that the adjacent distribution of red and blue is mainly due to the mixing of the fluids at small Sr [12,23]. As stratification parameter
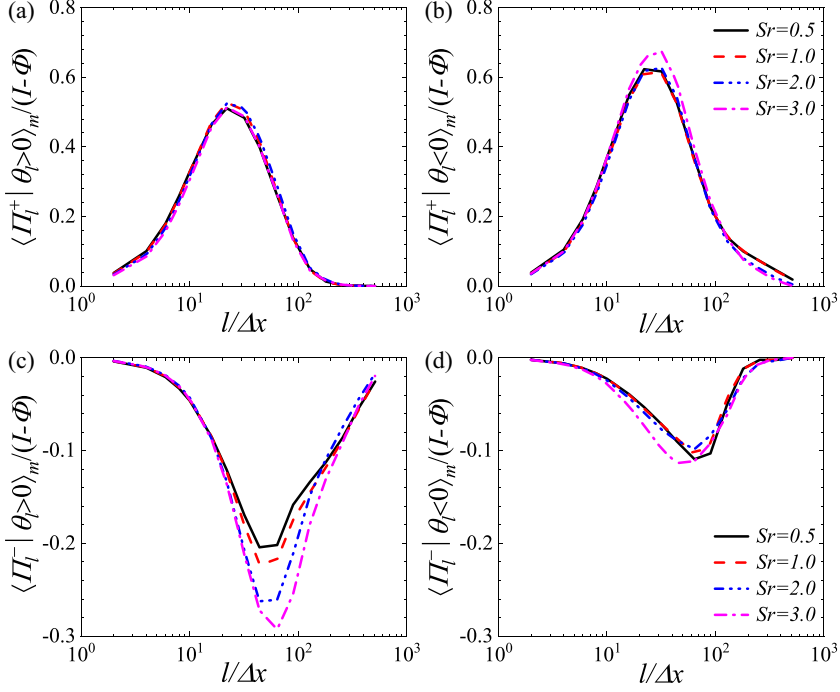
FIG. 19. Conditional average of the positive and negative components of SGS flux of kinetic energy at $t/\tau = 3.0$ for stratification parameters $Sr = 0.5, 1.0, 2.0, 3.0$: (a) $\langle \Pi_l^+ \mid \theta_l > 0 \rangle_m / (I - \Phi)$, (b) $\langle \Pi_l^+ \mid \theta_l < 0 \rangle_m / (I - \Phi)$, (c) $\langle \Pi_l^- \mid \theta_l > 0 \rangle_m / (I - \Phi)$, and (d) $\langle \Pi_l^- \mid \theta_l < 0 \rangle_m / (I - \Phi)$.

increases, the large expansion regions increase slightly, owing to strong expansion motions in the mixing layer [12].

Figure 21 displays the isosurfaces of SGS flux at $\Pi_l / \Pi_l' = -0.5$ for the filter width $l/\Delta x = 22$ at $t/\tau = 3.0$, for different stratification parameters $Sr = 0.5, 1.0, 2.0, 3.0$. The isosurfaces are colored based on the normalized filtered velocity divergence θ_l / θ_l'. The structures are more sparse, with smaller length scales, as compared with the isosurfaces $\Pi_l / \Pi_l' = 2.0$. The observations reveal that direct SGS flux is stronger than reverse SGS flux of kinetic energy, which is consistent with the statistical result in Fig. 18 and the results in compressible homogeneous isotropic turbulence [34]. At $Sr = 0.5$, the positive and negative θ_l / θ_l' are nearly equally distributed. The expansion motions increase gradually on the isosurfaces $\Pi_l / \Pi_l' = -0.5$ as stratification parameter increases. We see the larger structures of isosurfaces $\Pi_l / \Pi_l' = -0.5$ at $Sr = 3.0$, indicating that expansion motions enhance the reverse SGS flux of kinetic energy at large Sr, which is consistent with the statistical result in Fig. 19. In addition, we see that the both strong expansion motions and compression motions are mainly distributed in the upper half of the mixing layer at $Sr \geqslant 2.0$, which is different with isosurfaces $\Pi_l / \Pi_l' = 2.0$ in Fig. 20.

Figure 22 displays the average of normalized SGS flux $\Pi_l / (I - \Phi)$ conditioned on the normalized filtered velocity divergence θ_l / θ_l' at different filter widths $l/\Delta x = 16, 24, 32, 48$ for different stratification parameters $Sr = 0.5, 1.0, 2.0, 3.0$ at $t/\tau = 3.0$. In compression regions $\theta_l / \theta_l' < 0$, the conditional average of SGS flux $\langle \Pi_l / (I - \Phi) \mid \theta_l / \theta_l' \rangle$ is little affected by the filter width for $16 \leqslant l/\Delta x \leqslant 32$ at $Sr \leqslant 2.0$ and $16 \leqslant l/\Delta x \leqslant 48$ at $Sr = 3.0$, except the situation that the magnitude of filter width and velocity divergence are large due to the lack of samples. However, $\langle \Pi_l / (I - \Phi) \mid \theta_l / \theta_l' \rangle$ decreases as the filter width increases in expansion regions $\theta_l / \theta_l' > 0$. In addition, the conditional average of SGS flux becomes stronger in compression regions $\theta_l / \theta_l' < 0$
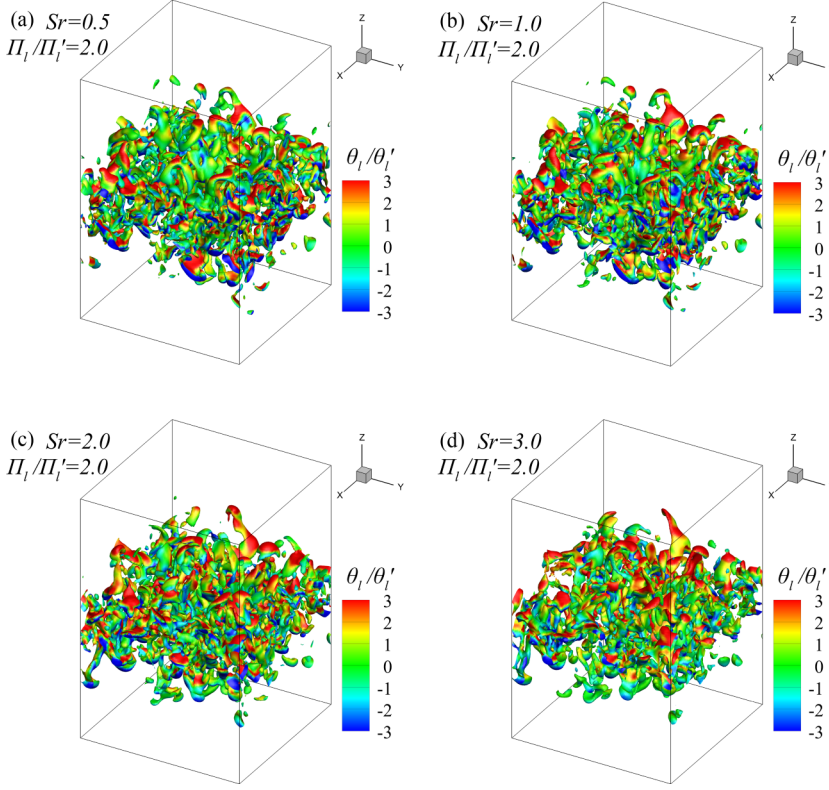
FIG. 20. Isosurfaces of SGS flux at $\Pi_l/\Pi_l' = 2.0$ for the filter width $l/\Delta x = 22$ at $t/\tau = 3.0$, for different stratification parameters (a) Sr = 0.5, (b) Sr = 1.0, (c) Sr = 2.0, and (d) Sr = 3.0.

and weaker in expansion regions $\theta_l/\theta_l' > 0$ with the increase of Sr, owing to that compression motions enhance direct SGS flux and the expansion motions strengthen the reverse SGS flux.

An algebraic relation for the conditional average of SGS flux $\langle \Pi_l/(I - \Phi) \mid \theta_l/\theta_l' \rangle$ in compression regions $\theta_l/\theta_l' < 0$ can be introduced:

$$\langle \Pi_l/(I - \Phi) \mid \theta_l/\theta_l' \rangle = \begin{cases} \alpha_1(\theta_l/\theta_l'), & \text{Sr} \leqslant 1.0, \\ \alpha_2(\theta_l/\theta_l')^2, & \text{Sr} \geqslant 2.0, \end{cases}$$

where $\alpha_1 = 0.6$ and $\alpha_2 = 0.23$. It is worth noting that this relation is better for $-4.0 \leqslant \theta_l/\theta_l' < 0$ and not good for $-6.0 \leqslant \theta_l/\theta_l' \leqslant -4.0$ at Sr = 2.0, which seems to be a transition between θ_l/θ_l' and $(\theta_l/\theta_l')^2$. The (θ_l/θ_l')-square scaling of $\langle \Pi_l/(I - \Phi) \mid \theta_l/\theta_l' \rangle$ is proposed at high turbulent Mach numbers $M_t \geqslant 0.6$ in compressible homogeneous isotropic turbulence by Wang *et al.* [34,53] and observed in compressible forced anisotropic turbulence [54]. However, the turbulent Mach numbers are only 0.192 for Sr = 2.0 and 0.214 for Sr = 3.0 at $t/\tau = 3.0$ in our numerical simulations.

SGS kinetic energy flux is a key physical quantity in LES of turbulence. If direct SGS flux is relatively large, the SGS model needs to provide sufficient dissipation. If reverse SGS flux is relatively large, the SGS model also needs to provide appropriate reverse SGS flux of kinetic energy. In addition, energy backscatter can cause simulations to become numerically unstable. The reverse SGS flux increases with the increase of Sr, especially in expansion regions. Moreover, the reverse SGS flux is more likely to occur in the upper half of the mixing layer, because the upward moving bubbles are expanded. This observation puts forward higher requirements for the SGS model of compressible RT turbulence. Some traditional models, such as Smagorinsky model based on eddy
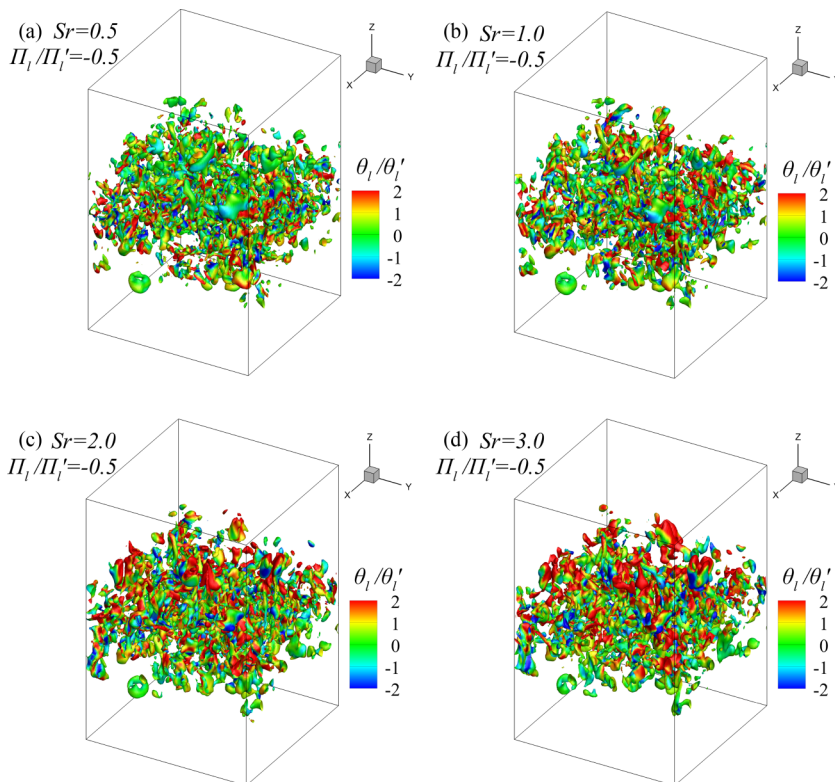
FIG. 21. Isosurfaces of SGS flux at $\Pi_l/\Pi_l' = -0.5$ for the filter width $l/\Delta x = 22$ at $t/\tau = 3.0$, for different stratification parameters (a) Sr = 0.5, (b) Sr = 1.0, (c) Sr = 2.0, and (d) Sr = 3.0.

viscosity hypothesis, are not suitable for computing energy backscatter. Therefore, it is necessary to develop highly accurate SGS models to simulate compressible RT turbulence, including dynamic spatial gradient models (DSGM) [55], dynamic iterative approximate deconvolution models (DIAD) [56], dynamic nonlinear algebraic models [57], and artificial-neural-network-based SGS models [58–64].

E. Large-scale pressure-dilatation term

In the filtered equation for the average of the large-scale kinetic energy of compressible flow, the average of the large-scale pressure-dilatation term $\langle \bar{p} \boldsymbol{\nabla} \cdot \widetilde{\mathbf{u}} \rangle$ can be decomposed to $\langle \bar{p} \boldsymbol{\nabla} \cdot \bar{\mathbf{u}} \rangle$ and $\langle \frac{1}{\bar{\rho}} \frac{\partial \bar{p}}{\partial x_j} (\overline{\rho u_j} - \bar{\rho} \bar{u}_j) \rangle$. The former is the mean pressure dilatation, which is almost flat as a function of filter width and affects only the large-scale dynamics in compressible RT turbulence [14,28]. The latter is the baropycnal work, transferring kinetic energy from large scales to small scales, which decays with filter width and becomes very little at small scales [14,28]. Although they are important in studying the physical mechanism of kinetic energy transfer, the filter variables $\bar{u}_j$, $\overline{\rho u_j}$, and $\boldsymbol{\nabla} \cdot \bar{\mathbf{u}}$ are not closed in the large eddy simulation (LES). In addition, they have been analyzed in detail in compressible RT turbulence [14,28]. Therefore, we mainly analyze the large-scale pressure-dilatation term $\bar{p} \boldsymbol{\nabla} \cdot \widetilde{\mathbf{u}}$ [34], which can be directly calculated from LES of compressible turbulence.

Figure 23 shows the normalized spatial average of the large-scale pressure-dilatation term $\langle \Phi_l \rangle / (I - \Phi)$ for different stratification parameters Sr at $t/\tau = 2.5, 3.0, 3.5$. We see that the curves of $\langle \Phi_l \rangle / (I - \Phi)$ as functions of filter width $l/\Delta x$ are similar at different Sr and times t/τ. $\langle \Phi_l \rangle / (I - \Phi)$ is approximately constant at small scales $l/\Delta x \leqslant 8$, which is small for Sr $\leqslant 1.0$
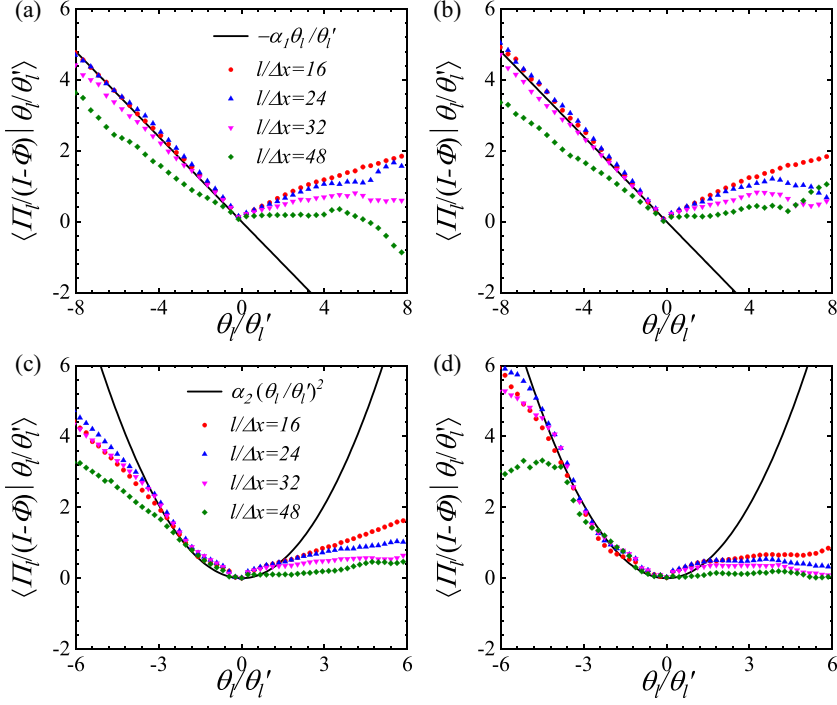
FIG. 22. Average of normalized SGS flux $\Pi_l/(I - \Phi)$ conditioned on the normalized filtered velocity divergence θ_l/θ_l' for different filter widths $l/\Delta x = 16, 24, 32, 48$ at $t/\tau = 3.0$ for different stratification parameters (a) Sr = 0.5, (b) Sr = 1.0, (c) Sr = 2.0, and (d) Sr = 3.0.

and has a relatively large negative value for Sr $\geqslant$ 2.0. It is worth noting that the positive value of $\langle \Phi_l \rangle/(I - \Phi)$ at large scales does not indicate the conversion of kinetic energy to internal energy for small Sr, which is due to that baropycnal work $\langle \frac{1}{\bar{\rho}} \frac{\partial \bar{p}}{\partial x_j} (\overline{\rho u_j} - \bar{\rho} \bar{u}_j) \rangle$ has a large positive value at large scales and converts kinetic energy from large scales to small scales [14,28]. However, $\langle \Phi_l \rangle/(I - \Phi)$ has a large negative value at small scales for large Sr, indicating that the internal energy is converted to kinetic energy at large scales [14,28]. Thus, the large-scale pressure-dilatation term is important in LES of compressible RT turbulence at large Sr.

Figure 24 displays the time evolution of average of the large-scale pressure-dilatation term $\langle \Phi_l \rangle/(I - \Phi)$ at given filter width $l/\Delta x = 4, 32, 128$ for different stratification parameters Sr. The changes of $\langle \Phi_l \rangle/(I - \Phi)$ at different filter width $l/\Delta x$ with time are similar for a given Sr, which
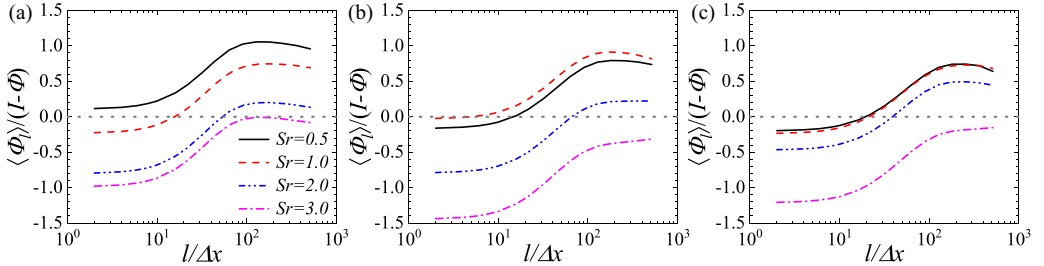

FIG. 23. Normalized average of large-scale pressure-dilatation term $\langle \Phi_l \rangle/(I - \Phi)$ for stratification parameters Sr = 0.5, 1.0, 2.0, 3.0 at different times: (a) $t/\tau = 2.5$, (b) $t/\tau = 3.0$, and (c) $t/\tau = 3.5$.
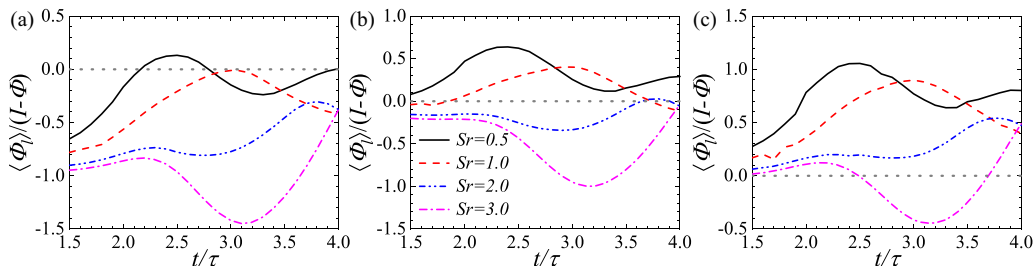
FIG. 24. Time evolution of the normalized average of large-scale pressure-dilatation term $\langle \Phi_l \rangle / (I - \Phi)$ at given filter width $l/\Delta x$ for stratification parameters Sr = 0.5, 1.0, 2.0, 3.0: (a) $\langle \Phi_l \rangle / (I - \Phi)$ at $l/\Delta x = 4$, (b) $\langle \Phi_l \rangle / (I - \Phi)$ at $l/\Delta x = 32$ and (c) $\langle \Phi_l \rangle / (I - \Phi)$ at $l/\Delta x = 128$.

are consistent with the fact that the curves of $\langle \Phi_l \rangle / (I - \Phi)$ as functions of filter width are parallel to each other in Fig. 23. Overall, their values decrease with the increase of Sr. $\langle \Phi_l \rangle$ at small scale $l/\Delta x = 4$ is approximately equal to $\langle \bar{p} \nabla \cdot \bar{\mathbf{u}} \rangle$, owing to the baropycnal work is close to 0 at small scales[14,28]. Therefore, $\langle \Phi_l \rangle / (I - \Phi)$ at $l/\Delta x = 4$ is basically consistent with $-\Phi/(I - \Phi)$ shown in Fig. 12.

The root-mean-square values of large-scale pressure-dilatation term are defined as $\Phi_l' = \sqrt{\langle (\Phi_l - \langle \Phi_l \rangle_{xy})^2 \rangle}$. We plot Φ_l' at $t/\tau = 3.0$ and at a given filter width $l/\Delta x = 32$ in Fig. 25. Φ_l' basically keeps constant at small scales $l/\Delta x \leqslant 20$ and nearly decreases in the form of power function of the filter width at $l/\Delta x > 50$. In addition, The curves of Φ_l' are parallel to each other. Φ_l' at $l/\Delta x = 32$ increases with time at $t/\tau < 2.0$ and is almost constant at $t/\tau > 2.0$. The values of the r.m.s. values of pressure-dilatation at a given filter width decrease with the increase of Sr.

VI. CONCLUSIONS

In this paper, numerical simulations of 3D compressible Rayleigh-Taylor turbulence are carried out for isothermal background stratification at Atwood number $A_t = 0.5$ and stratification parameters Sr = 0.5, 1.0, 2.0, 3.0, corresponding to different flow compressibility. The effects of stratification parameters on bubble heights are different for different definitions, which is due to that the bubbles become bigger for large Sr. Meanwhile, the different shape of bubbles also affects the different vertical height molecular mixing degree for different Sr, although the total molecular
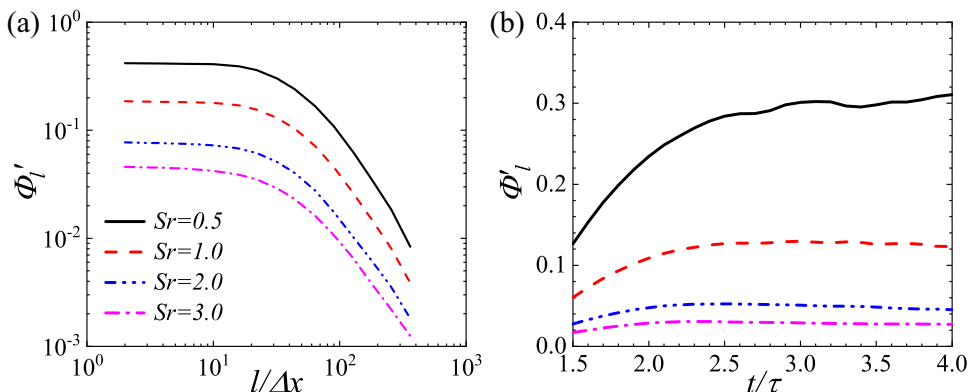

FIG. 25. (a) The r.m.s. values of large-scale pressure-dilatation Φ_l' at $t/\tau = 3.0$ and (b) the time evolution of the r.m.s. values of large-scale pressure-dilatation at filter width $l/\Delta x = 32$ at stratification parameters Sr = 0.5, 1.0, 2.0, 3.0.
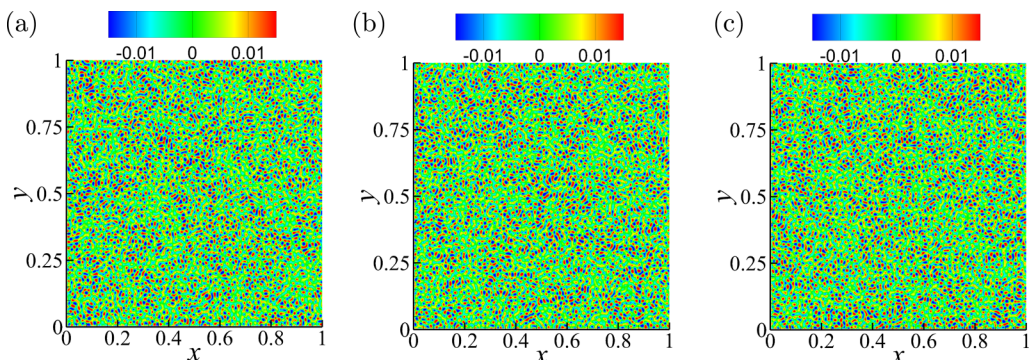
FIG. 26. Three initial perturbation displacement z_0: (a) I.C.a, $40 \leqslant k = \sqrt{k_x^2 + k_y^2} \leqslant 64$, (b) I.C.b, $40 \leqslant k = \sqrt{k_x^2 + k_y^2} \leqslant 64$, and (c) I.C.c, $30 \leqslant k = \sqrt{k_x^2 + k_y^2} \leqslant 45$.

mixing degree averaged in the mixing layer is independent of Sr. In addition, the bubble heights also increase rapidly at large Sr because of the conversion of internal energy to kinetic energy.

Flow compressibility plays an important role in the production of kinetic energy at large scales, which comes from two sources: the conversion of potential energy and conversion of internal energy through pressure-dilatation work. Whether they act as sources or sinks depend on the stratification parameters Sr. At small Sr, kinetic energy mainly comes from potential energy, while the conversion of internal energy to kinetic energy may play the role of source or sink at a given time. On the contrary, internal energy is the main source at large Sr. The conversion of kinetic energy to potential energy occurs, owing to the initial exponential density stratification. Therefore, with the increase of Sr, the ratio of released potential energy to kinetic energy ($-\Delta\mathrm{PE}/\mathrm{KE}$) decreases from 2 to a negative value, while the ratio of released internal energy to kinetic energy ($-\Delta\mathrm{IE}/\mathrm{KE}$) increases from -1 to a value greater than 1.

The injected kinetic energy at large scales is transferred from large scales to small scales through deformation work (SGS flux Π_l) and baropycnal work. The overall statistical properties of normalized SGS flux of kinetic energy are basically independent of Sr. The reverse SGS flux increases with increase of Sr, but it tends to appear at the larger scales and is much weaker at middle scales than the direct SGS flux. The compression motions enhance direct SGS flux of kinetic energy from large scales to small scales, while the expansion motions strengthen the reverse SGS flux of kinetic energy from small scales to large scales. The average of normalized SGS flux conditioned on the filtered velocity divergence is nearly independent of filter width for $16 \leqslant l/\Delta x \leqslant 32$ in compression
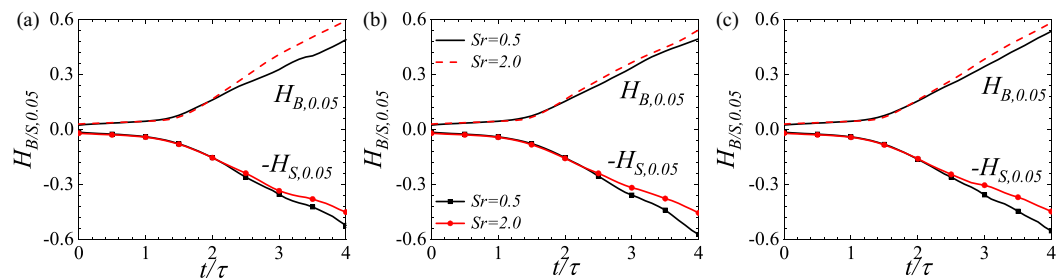

FIG. 27. Time evolution of spike and bubble heights using the 5% threshold values at stratification parameters Sr = 0.5, 2.0 and Reynolds number Re = 10000: (a) I.C.a, $40 \leqslant k = \sqrt{k_x^2 + k_y^2} \leqslant 64$, (b) I.C.b, $40 \leqslant k = \sqrt{k_x^2 + k_y^2} \leqslant 64$, and (c) I.C.c, $30 \leqslant k = \sqrt{k_x^2 + k_y^2} \leqslant 45$.
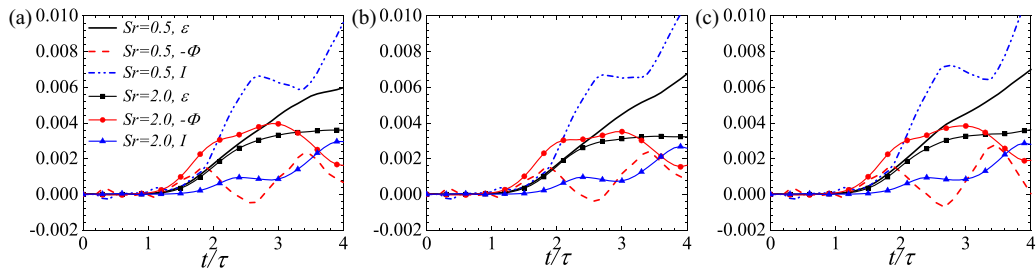
FIG. 28. Time evolution of the terms in the equation of kinetic energy at stratification parameters Sr = 0.5, 2.0 and Reynolds number Re = 10 000: (a) I.C.a, $40 \leqslant k = \sqrt{k_x^2 + k_y^2} \leqslant 64$, (b) I.C.b, $40 \leqslant k = \sqrt{k_x^2 + k_y^2} \leqslant 64$, and (c) I.C.c, $30 \leqslant k = \sqrt{k_x^2 + k_y^2} \leqslant 45$.

regions, which is nearly proportional to the filtered velocity divergence θ_l/θ_l' at Sr $\leqslant 1.0$ and the square of θ_l/θ_l' at Sr > 2.0. In addition, the net upscale cascade at large scales only exists in the expansion regions, owing to the strong reverse SGS flux of kinetic energy. The kinetic energy at small scales is eventually dissipated through viscosity and is converted to internal energy. The normalized average of viscous dissipation term $\varepsilon_l/\varepsilon$ is almost independent of Sr.

The normalized average values of the large-scale pressure-dilatation $\langle \Phi_l \rangle/(I - \Phi)$ are similar for different Sr and different times t/τ. Overall, their values decrease with the increase of Sr. $\langle \Phi_l \rangle/(I - \Phi)$ has a relatively large negative value at small scales $l/\Delta x \leqslant 8$ for large Sr, which can play an important role in LES of compressible RT turbulence. The present results are helpful for developing advanced LES models in compressible RT turbulence.

APPENDIX: EFFECTS OF INITIAL PERTURBATION ON COMPRESSIBLE RT TURBULENCE

Three initial perturbation displacement fields z_0 are randomly generated and shown in Fig. 26. We numerically simulate RT turbulence at Reynolds number Re = 10 000 and stratification parameters Sr = 0.5, 2.0 with $256^2 \times 512$ grid points in a rectangular box of $L_r^2 \times 2L_r$ ($[-L_r, L_r]$), where $L_r = 1.0$. The mesh Grashoff numbers Gr_Δ is 5.96. The spike and bubble heights using the 5% threshold values are shown in Fig. 27. Figure 28 presents the time evolution of each term in equation of kinetic energy (19). It is observed that the initial perturbation displacement fields have a negligible effect on the numerical results.

---

[1] J. D. Kilkenny, S. G. Glendinning, S. W. Haan, B. A. Hammel, J. D. Lindl, D. Munro, B. A. Remington, S. V. Weber, J. P. Knauer, and C. P. Verdon, A review of the ablative stabilization of the Rayleigh-Taylor instability in regimes relevant to inertial confinement fusion, Phys. Plasmas **1**, 1379 (1994).

[2] R. D. Petrasso, Inertial fusion—Rayleigh's challenge endures, Nature **367**, 217 (1994).

[3] W. Hillebrandt and J. C. Niemeyer, Type Ia supernova explosion models, Annu. Rev. Astron. Astrophys. **38**, 191 (2000).

[4] A. Burrows, Supernova explosions in the universe, Nature **403**, 727 (2000).

[5] S. Gauthier and B. Le Creurer, Compressibility effects in Rayleigh-Taylor instability-induced flows, Philos. Trans. R. Soc. A **368**, 1681 (2010).

[6] Y. Zhou, Rayleigh-Taylor and Richtmyer-Meshkov instability induced flow, turbulence, and mixing. II, Phys. Rep. **723-725**, 1 (2017).

[7] T. Luo, J. Wang, C. Xie, M. Wan, and S. Chen, Effects of compressibility and Atwood number on the single-mode Rayleigh-Taylor instability, Phys. Fluids **32**, 012110 (2020).

[8] S. J. Reckinger, D. Livescu, and O. V. Vasilyev, Comprehensive numerical methodology for direct numerical simulations of compressible Rayleigh-Taylor instability, J. Comput. Phys. **313**, 181 (2016).

[9] D. Livescu, Compressibility effects on the Rayleigh-Taylor instability growth between immiscible fluids, Phys. Fluids **16**, 118 (2004).

[10] S. Gauthier, Compressible Rayleigh-Taylor turbulent mixing layer between newtonian miscible fluids, J. Fluid Mech. **830**, 211 (2017).

[11] M. A. Lafay, B. Le Creurer, and S. Gauthier, Compressibility effects on the Rayleigh-Taylor instability between miscible fluids, Europhys. Lett. **79**, 64002 (2007).

[12] T. Luo and J. Wang, Effects of Atwood number and stratification parameter on compressible multimode Rayleigh-Taylor instability, Phys. Fluids **33**, 115111 (2021).

[13] S. A. Wieland, S. J. Reckinger, P. E Hamlington, and D. Livescu, Effects of background stratification on the compressible Rayleigh-Taylor instability, in *Proceedings of the 47th AIAA Fluid Dynamics Conference* (AIAA, Reston, VA, 2017), p. 3974

[14] D. Zhao, R. Betti, and H. Aluie, Scale interactions and anisotropy in Rayleigh-Taylor turbulence, J. Fluid Mech. **930**, A29 (2022).

[15] S. K. Lele, Compressibility effects on turbulence, Annu. Rev. Fluid Mech. **26**, 211 (1994).

[16] J. Wang, T. Gotoh, and T. Watanabe, Scaling and intermittency in compressible isotropic turbulence, Phys. Rev. Fluids **2**, 053401 (2017).

[17] D. A. Donzis and J. P. John, Universality and scaling in homogeneous compressible turbulence, Phys. Rev. Fluids **5**, 084609 (2020).

[18] C. Q. Fu, Z. Zhao, X. Xu, P. Wang, N. S. Liu, Z. H. Wan, and X. Y. Lu, Nonlinear saturation of bubble evolution in a two-dimensional single-mode stratified compressible Rayleigh-Taylor instability, Phys. Rev. Fluids **7**, 023902 (2022).

[19] E. George and J. Glimm, Self-similarity of Rayleigh-Taylor mixing rates, Phys. Fluids **17**, 054101 (2005).

[20] H. Jin, X. F. Liu, T. Lu, B. Cheng, J. Glimm, and D. H. Sharp, Rayleigh-Taylor mixing rates for compressible flow, Phys. Fluids **17**, 024104 (2005).

[21] S. Gauthier, Compressibility effects in Rayleigh-Taylor flows: Influence of the stratification, Phys. Scr. **2013**, T155 (2013).

[22] A. W. Cook and Y. Zhou, Energy transfer in Rayleigh-Taylor instability, Phys. Rev. E **66**, 026312 (2002).

[23] A. W. Cook and P. E. Dimotakis, Transition stages of Rayleigh-Taylor instability between miscible fluids, J. Fluid Mech. **443**, 69 (2001).

[24] W. H. Cabot and A. W. Cook, Reynolds number effects on Rayleigh-Taylor instability with possible implications for type-Ia supernovae, Nat. Phys. **2**, 562 (2006).

[25] W. Cabot, Comparison of two- and three-dimensional simulations of miscible Rayleigh-Taylor instability, Phys. Fluids **18**, 045101 (2006).

[26] D. L. Youngs, Numerical-simulation of mixing by Rayleigh-Taylor and Richtmyer-Meshkov instabilities, Laser Part. Beams **12**, 725 (1994).

[27] Q. Zhou, Y. Huang, Z. Lu, Y. Liu, and R. Ni, Scale-to-scale energy and enstrophy transport in two-dimensional Rayleigh-Taylor turbulence, J. Fluid Mech. **786**, 294 (2016).

[28] Z. Zhao, N. Liu, and X. Lu, Kinetic energy and enstrophy transfer in compressible Rayleigh-Taylor turbulence, J. Fluid Mech. **904**, A37 (2020).

[29] H. Aluie, Scale decomposition in compressible turbulence, Physica D **247**, 54 (2013).

[30] D. Zhao and H. Aluie, Inviscid criterion for decomposing scales, Phys. Rev. Fluids **3**, 054603 (2018).

[31] P. Chassaing, An alternative formulation of the equations of turbulent motion for a fluid of variable density, J. Mech. Theor. Appl. **4**, 375 (1985).

[32] G. C. Burton, Study of ultrahigh Atwood-number Rayleigh-Taylor mixing dynamics using the nonlinear large-eddy simulation method, Phys. Fluids **23**, 045106 (2011).

[33] S. Kida and S. A Orszag, Energy and spectral dynamics in forced compressible turbulence, J. Sci. Comput. **5**, 85 (1990).

[34] J. Wang, M. Wan, S. Chen, and S. Chen, Kinetic energy transfer in compressible isotropic turbulence, J. Fluid Mech. **841**, 581 (2018).

[35] G. Dimonte, D. L. Youngs, A. Dimits, S. Weber, M. Marinak, S. Wunsch, C. Garasi, A. Robinson, M. J. Andrews, P. Ramaprabhu, A. C. Calder, B. Fryxell, J. Biello, L. Dursi, P. MacNeice, K. Olson, P. Ricker, R. Rosner, F. Timmes, H. Tufo *et al.*, A comparative study of the turbulent Rayleigh-Taylor instability using high-resolution three-dimensional numerical simulations: The alpha-group collaboration, Phys. Fluids **16**, 1668 (2004).

[36] P. Ramaprabhu, G. Dimonte, and M. J. Andrews, A numerical study of the influence of initial perturbations on the turbulent Rayleigh-Taylor instability, J. Fluid Mech. **536**, 285 (2005).

[37] D. L. Youngs, The density ratio dependence of self-similar Rayleigh-Taylor mixing, Philos. Trans. R. Soc. A **371**, 20120173 (2013).

[38] S. K. Lele, Compact finite-difference schemes with spectral-like resolution, J. Comput. Phys. **103**, 16 (1992).

[39] J. Wang, L. P. Wang, Z. Xiao, Y. Shi, and S. Chen, A hybrid numerical simulation of isotropic compressible turbulence, J. Comput. Phys. **229**, 5257 (2010).

[40] C. W. Shu and S. Osher, Efficient implementation of essentially nonoscillatory shock-capturing schemes, J. Comput. Phys. **77**, 439 (1988).

[41] B. J. Olson and A. W. Cook, Rayleigh-Taylor shock waves, Phys. Fluids **19**, 128108 (2007).

[42] D. Livescu, J. R. Ristorcelli, M. R. Petersen, and R. A. Gore, New phenomena in variable-density Rayleigh-Taylor turbulence, Phys. Scr. **2010**, 014015 (2010).

[43] Y. Zhou and W. H. Cabot, Time-dependent study of anisotropy in Rayleigh-Taylor instability induced turbulent flows with a variety of density ratios, Phys. Fluids **31**, 084106 (2019).

[44] D. Livescu, J. R. Ristorcelli, R. A. Gore, S. H. Dean, W. H. Cabot, and A. W. Cook, High-Reynolds number Rayleigh-Taylor turbulence, J. Turbul. **10**, N13 (2009).

[45] A. G. W. Lawrie and S. B. Dalziel, Rayleigh–taylor mixing in an otherwise stable stratification, J. Fluid Mech. **688**, 507 (2011).

[46] M. S. Davies Wykes and S. B. Dalziel, Efficient mixing in stratified flows: Experimental study of a Rayleigh-Taylor unstable interface within an otherwise stable stratification, J. Fluid Mech. **756**, 1027 (2014).

[47] R. J. R. Williams, Rayleigh-Taylor mixing between density stratified layers, J. Fluid Mech. **810**, 584 (2017).

[48] Y. S. Zhang, W. D. Ni, Y. C. Ruan, and H. S. Xie, Quantifying mixing of Rayleigh-Taylor turbulence, Phys. Rev. Fluids **5**, 104501 (2020).

[49] A. W. Cook, W. Cabot, and P. L. Miller, The mixing transition in Rayleigh-Taylor instability, J. Fluid Mech. **511**, 333 (2004).

[50] J. Wang, Y. Shi, L. P. Wang, Z. Xiao, X. T. He, and S. Chen, Effect of compressibility on the small-scale structures in isotropic turbulence, J. Fluid Mech. **713**, 588 (2012).

[51] M. P. Martin, U. Piomelli, and G. V. Candler, Subgrid-scale models for compressible large-eddy simulations, Theor. Comput. Fluid Dyn. **13**, 361 (2000).

[52] H. Aluie, Compressible Turbulence: The Cascade and its Locality, Phys. Rev. Lett. **106**, 174502 (2011).

[53] J. Wang, Y. Yang, Y. Shi, Z. Xiao, X. T. He, and S. Chen, Cascade of Kinetic Energy in Three-Dimensional Compressible Turbulence, Phys. Rev. Lett. **110**, 214505 (2013).

[54] X. Wang, J. Wang, H. Li, and S. Chen, Kinetic energy transfer in compressible homogeneous anisotropic turbulence, Phys. Rev. Fluids **6**, 064601 (2021).

[55] Y. Wang, Z. Yuan, C. Xie, and J. Wang, A dynamic spatial gradient model for the subgrid closure in large-eddy simulation of turbulence, Phys. Fluids **33**, 075119 (2021).

[56] Z. Yuan, Y. Wang, C. Xie, and J. Wang, Dynamic iterative approximate deconvolution models for large-eddy simulation of turbulence, Phys. Fluids **33**, 085125 (2021).

[57] Z. Yuan, Y. Wang, C. Xie, and J. Wang, Dynamic nonlinear algebraic models with scale-similarity dynamic procedure for large-eddy simulation of turbulence, Adv. Aerodyn. **4**, 16 (2022).

[58] M. Gamahara and Y. Hattori, Searching for turbulence models by artificial neural network, Phys. Rev. Fluids **2**, 054604 (2017).

[59] X. I. A. Yang, S. Zafar, J.-X. Wang, and H. Xiao, Predictive large-eddy-simulation wall modeling via physics-informed neural networks, Phys. Rev. Fluids **4**, 034602 (2019).

[60] C. Xie, K. Li, C. Ma, and J. Wang, Modeling subgrid-scale force and divergence of heat flux of compressible isotropic turbulence by artificial neural network, Phys. Rev. Fluids **4**, 104605 (2019).

[61] C. Xie, J. Wang, and W. E, Modeling subgrid-scale forces by spatial artificial neural networks in large eddy simulation of turbulence, Phys. Rev. Fluids **5**, 054606 (2020).

[62] Z. Yuan, C. Xie, and J. Wang, Deconvolutional artificial neural network models for large eddy simulation of turbulence, Phys. Fluids **32**, 115106 (2020).

[63] J. Park and H. Choi, Toward neural-network-based large eddy simulation: Application to turbulent channel flow, J. Fluid Mech. **914**, A16 (2021).

[64] Y. Wang, Z. Yuan, C. Xie, and J. Wang, Artificial neural network-based spatial gradient models for large-eddy simulation of turbulence, AIP Adv. **11**, 055216 (2021).